THE $B^0 \to \omega\pi^0$ DIFFERENTIAL CROSS SECTION

by

Paul J. Brockman

A thesis submitted to the Faculty of Graduate Studies and Research in partial fulfillment of the requirements for the degree of Master of Science.

Department of Physics
McGill University
Montréal, Québec
Canada

August 1978

© Paul J. Brockman 1978

To Patricia for her patience

and

to my parents for their encouragement.

ABSTRACT

The differential cross section for B^0 production in the reaction $\pi^- p \to B^0 n$, at an incident beam momentum of 8.45 GeV/c, has been measured in a counter-spark chamber experiment at the Zero Gradient Synchrotron of Argonne National Laboratory. Results are presented for a sample of 1781 events. The B^0 cross section shows no sign of the forward turnover predicted on the basis of A_2 exchange.

RESUME

La section efficace différentielle pour la formation de B^0 dans la réaction $\pi^- p \to B^0 n$, à une impulsion incidente de 8.45 GeV/c, a été mesurée dans une expérience exécutée au synchroton du Argonne National Laboratory. Nous présentons les résultats pour un échantillon de 1781 événements. La section efficace différentielle de B^0 ne démontre pas le "trou" vers l'avant prédit sous la présomption d'échange de A_2.

ACKNOWLEDGEMENTS

I wish to thank P.M. Patel, J.F. Martin and M.H. Shaevitz for their assistance in this experiment.

My thanks also to N.R. Stanton for his time and helpful advice.

I would also like to thank the following people for their help in running shifts or their assistance in the analysis: J. Dankowych, J.W. Heimaster, C.J. Zanfino, K. Edwards, E. Gandsman, D. Legacy, A.J. Pawlicki, J.D. Prentice and E. Shabazian.

Finally I want to express my appreciation to the Argonne National Laboratory ZGS operations crew and H. Coombes, J. Fitch, A. Kiang and C. Rush for their technical support.

TABLE OF CONTENTS

INTRODUCTION

This thesis presents the first observation of the B^0 axial vector meson via the decay $B^0 \to \omega\pi^0$ in the reaction

$$\pi^- p \to B^0 n$$
$$\quad\downarrow \omega\pi^0$$
$$\quad\quad\downarrow \gamma\gamma$$
$$\quad\quad\downarrow \pi^+\pi^-\pi^0$$
$$\quad\quad\quad\downarrow \gamma\gamma \ .$$

The differential cross section of the process $B^0 \to \omega\pi^0$ is also calculated.

The data for this reaction were taken at the Argonne National Laboratory Zero Gradient Synchrotron in a high statistics ($> 8 \times 10^6$ triggers) counter-spark chamber experiment (E-397)[1] using incident pions of momentum 8.45 GeV/c.

A description of the experiment will be given in Part I. We will discuss the details of the data analysis and present our final results in Part II.

PART I

EXPERIMENTAL APPARATUS

CHAPTER 1
APPARATUS

Our sample of events from the process

$$\pi^- p \to \pi^+\pi^-\pi^0\pi^0 n, \quad \pi^0 \to \gamma\gamma, \quad \pi^0 \to \gamma\gamma$$

(hereafter referred to as 4γ events) was obtained simultaneously with the collection of data for study of the reactions

$$\pi^- p \to \pi^+\pi^-\pi^0 n, \quad \pi^0 \to \gamma\gamma$$

and

$$\pi^- p \to \pi^+\pi^-\eta\, n, \quad \eta \to \gamma\gamma$$

using an incident π^- beam of momentum 8.45 GeV/c at the ZGS in December, 1975 and April, 1976.

For the reaction

(I.1) $$\pi^- p \to B^0 n, \quad B^0 \to \omega\pi^0, \quad \omega \to \gamma\gamma, \quad \omega \to \pi^+\pi^-\pi^0, \quad \pi^0 \to \gamma\gamma$$

all the final B^0 decay products were detected: the charged particles, using a conventional dipole magnet forward spectrometer (ten spark chambers); and the gamma rays, by means of an array of 56 lead glass blocks preceded by three spark chambers. The neutron was not detected. The experimental layout is shown in Figure 1 and discussed in detail in the following sections.

§1.A. Beam

The pion beam (see Figure 2) was produced by directing 12 GeV/c protons at a beryllium target in the Extracted Proton Beam II of the ZGS. Negative particles produced at 1½ degrees were focused by a two-stage beam transport system onto horizontal and vertical beam veto scintillation counters, BV1 and BV2, situated 120 inches downstream of the liquid hydrogen target.

The first stage produced a momentum dispersed focus at the position of the beam counter hodoscope BH - a set of seven finger counters, each subtending a momentum bite of ½% FWB. The second stage recombined the momenta, focusing the beam onto the BV1 and BV2 counters, where all non-interacting beam events were rejected. Beam particles outside the one inch radius hydrogen target were removed by the hole anti-counter BHR + BHL. We averaged 60,000 beam particles per pulse, of which 85% passed within the hole.

The beam particle direction was determined by means of four magnetostrictive readout spark chambers, spaced 36 inches apart upstream of the hydrogen target. The slope and intercept of each trajectory were measured to within ±.1 mrad and ±.015 inches (FWHM), respectively. A summary of the beam characteristics is given in Table 1.

§1.B. Charged Particle Spectrometer

The charged particles' momenta were measured by means of a spectrometer located immediately downstream of the hydrogen target and HØ. It consisted of a set of five magnetostrictive readout spark chambers on either side of a wide aperture magnet (SCM104), with a gap 40 inches high by 60 inches wide by 32 inches deep. The magnet current was set to produce a central field of 5.9 kilogauss, with an integrated field of 240 kg-in. The thinness of the magnet, combined with the close positioning of the chambers to it, permitted a good acceptance for wide angle tracks.

Details of the charged particle detection equipment and spark chamber dimensions are listed in Table 2. A 5 KV pulse was applied to the chambers for each trigger sensed. This was done using thyratron-capacitor bank units. A potential of 75 VDC was maintained on all chambers to help clear away the ionized debris from stray charged tracks. In addition to this, a 1 KV, 600 nsec pulse was applied after each trigger to remove residual ionization from the sparks.

The gas in the chambers was a mixture of 90% neon and 10% helium. Ethyl alcohol was added to the gas to quench the sparks. The entire gas system was recirculated and purified through a "Berkeley gas cart" system[3].

To eliminate the ambiguities which arise when multiple sparks occur, two chambers upstream and two chambers downstream were rotated by 45 degrees and 15 degrees respectively. Spark positions in the chambers were obtained by magnetostrictive wire readouts, using a Science Accessories Corporation (SAC) scaler system interfaced to CAMAC. Each plane was instrumented to handle up to four sparks.

§1.C. Photon Detector

The gamma rays were detected, and their energies determined, using a system of lead glass Cerenkov counters and magnetostrictive readout spark chambers.

The part of the detector which measured the position of the shower origin consisted of a lead sheet, 1.6 radiation lengths wide (conversion probability = 67%), followed by three spark chambers, two of which were rotated 12½ degrees to resolve multi-track ambiguities. These spark chambers were closely spaced, with a gap of only ¼ inch between the lead and the first chamber. Thus, the tightly collimated showers (rms angle per stage is ~ .2° for E = 1 GeV photons[2]) resulted in a single spark position which was taken as the shower conversion center. The position resolution was measured using electrons transported to the detector in a test beam, with the result Δx = .3" (FWHM) holding for all energies from 800 MeV to 2.5 GeV. This result applied also to incident photons because of the very small lateral spread of the secondary electrons. The second and third spark chambers supplied information for showers which were missed by the first spark chamber, and were also used to confirm and resolve shower positions. To ensure high efficiency for multi-spark events, each plane was instrumented to handle up to 8-12 sparks. For these chambers, the spark digitization was performed by Borer scalers interfaced to our CAMAC system.

The energies were measured using a 56-element lead glass array placed immediately downstream of the gamma chambers. The lead glass blocks were arranged in a symmetric array with a small beam hole (Figure 3). Each block measured 7½ inches by 7½ inches by 12 inches (10 radiation lengths) and was viewed by a 5 inch photomultiplier attached to the downstream face. The signal from each tube

was digitized by an Analog to Digital Converter (ADC) and the information made available to the online computer via CAMAC. The ADC reading, corrected for small geometrical losses, was then proportional to the energy deposited in the block. The measured energy resolution for a 2 GeV gamma shower was 18% FWHM.

§1.D. Anti-counter System

Events accompanied by charged particles or gamma rays that would go undetected by the apparatus were removed by an anti-counter system.

To reject gamma rays and charged particles recoiling at wide angles, the four lateral sides of the hydrogen target were covered by four alternate layers of 1/8 inch scintillator and 1/4 inch lead sheets. This target anti-counter (TA) setup is shown in detail in Figure 4. Events were rejected if one or more counters detected a particle. Also, part of the data (~19%) was taken with the less stringent constraint that the event was rejected if two or more of the anti-counters were set. All target anti-counters were latched and recorded with each event to allow the offline investigation of the above TA veto constraint; in particular, to correct for the loss resulting from good events being vetoed by recoil neutrons.

In the forward direction, the two sets of counters, AA1 and AA2 (Figure 1), limited the allowed solid angle to that covered by the spark chambers and the gamma ray detector. Each set of counters was made sensitive to gamma rays by covering its upstream side with ¼ inch lead sheets. Events were rejected if one of these counters detected a particle.

§1.E. Fast Logic and Trigger System

A system of scintillation counters was set up to detect, and isolate from unwanted background, all events consisting of two or three charged pions, two or more gamma rays, and a slow recoil neutron. Table 3 lists all counters. Signals from all counters concerned were combined in fast electronic logic modules to produce a trigger. The trigger was then used to initiate the firing of the spark chambers, the gating of the gamma shower ADC's, and the storing of the resulting CAMAC information.

The fast logic initiated an event trigger when a true condition resulted for the expression

$$\text{BEAM} \cdot \text{H}\emptyset \cdot \text{CHARGED} \cdot \text{GAMMA} \cdot \text{ANTI},$$

where each term is described below. A simplified trigger diagram is shown in Figure 5.

1) $\text{BEAM} = \text{S1} \cdot \text{B1} \cdot \text{B2} \cdot \overline{(\text{BHR} + \text{BHL})} \cdot \overline{(\text{BV1} + \text{BV2})}$

A beam particle, indicated by a count in each of the counters S1, B1, and B2 and none in the halo-counters BHR, BHL, must have interacted in the target because no counts occurred in the beam veto counters, BV1 and BV2.

2) HØ

The HØ counter, immediately downstream of the target, had a 1 inch radius hole centered on the beam. We demanded that at least one charged particle fire HØ to avoid false triggers caused by back-scatters from the lead converter triggering the H2 hodoscope. Monte Carlo simulation showed that at least one charged pion per event left the target at 4 degrees and fired HØ, for every B° event in our kinematic domain.

3) CHARGED = H2

We also demanded that exactly two or three elements of the 30 element scintillator hodoscope H2, located downstream of the last spectrometer chamber, be set off. In the less stringent "loose trigger" mode of data collection, the H2 constraint was relaxed to the requirement that two or more particles be present after the magnet, to permit the offline investigation of the effects of the H2 constraint. In particular, we wanted to study the losses due to false triggers caused by back-scatters from the lead converter immediately downstream of H2 (the HØ counter was not 100% effective in eliminating such false triggers).

4) $\text{GAMMA} = \overline{\text{GHF}} \cdot \text{GHR} \ (\geq 2)$

The gamma trigger was supplied by two identical 16-element scintillator hodoscopes, GHF and GHR, on either side of the spark chamber-lead converter "sandwich". A shower was indicated by a count in an element of GHR with no count in the corresponding element of GHF. At least two such "no-yes" combinations were required to initiate a gamma trigger. Again, some of the data was recorded under a looser "1γ-trigger" (~22%) to permit offline investigation of the losses due to the normal gamma trigger.

5) $\text{ANTI} = \overline{\text{AA1} + \text{AA2} + \text{TA}\ (\geq 1)}$

There were to be no counts in any anti-counter. In the "loose trigger" mode, the TA requirement was relaxed to the condition TA (≥2).

PART II

DATA ANALYSIS

CHAPTER 1

DATA COLLECTION AND RECONSTRUCTION ANALYSIS

§1.A. Online Data Collection and Analysis

Data acquisition and online analysis were performed on a General Automation SPC 16/85 computer interfaced to the experiment through a standard CAMAC network. The raw data for each event was stored in an event buffer consisting of 260 16-bit words. The collection system was capable of recording up to forty events per 600 msec ZGS pulse. All raw data were recorded on magnetic tape for later off-line analysis.

Approximately thirty percent of the recorded events were analyzed online during the 4-second intervals between ZGS pulses. This provided a valuable means of monitoring the performance of the apparatus. All spark chamber efficiencies, scintillation counter participations, and lead glass block participations were readily available for a continuous and rapid check of the equipment performance.

§1.B. Calibration Data

a) Spectrometer Data:

To determine the exact spatial position of each chamber, the spectrometer chambers were fired and data recorded for a non-interacting beam event at the start of each ZGS pulse. This information was used in the offline analysis as a check on the surveyed positions of the spark chambers.

Also, the distance between the rear and front fiducials was monitored, thus allowing the distance per scaler count to be updated for each magnetostrictive ribbon. This updating corrected for the aging of the ribbons and any temperature effects.

b) Lead Glass Blocks:

The energy deposited in each lead glass block was proportional to the ADC digitization readings. However, the proportionality constant varied due to changes in the photomultiplier tube gain; these were caused largely by shifts in ambient temperature. To monitor the relative gain drifts between tubes, the light output from a nitrogen laser was piped to each block via fiber optics. Laser pulse height data were recorded at the start of each ZGS pulse, and then

used by the offline analysis program to update the gains on a run-to-run basis. Twice daily, the laser pulse heights were recorded and utilized by the online analysis program to remove drifts.

An absolute calibration of each block was obtained by comparing the known π^0 mass to the mass of the 400,000 π^0 decays recorded during data-taking. The dominant contribution to the error in the π^0 mass measurement came from the uncertainty in the shower energies. The gain of each tube was therefore corrected by the method outlined in Figure 6. Briefly, for all two-gamma shower events, a digamma mass distribution was formed for each block, with the histogram of each block being incremented whenever it was the center for one of the two showers. The ratio of the centroid of each block's histogram to the actual π^0 mass was then calculated and used to correct the tube gains. This process was done at the end of the month's run.

§1.C. Offline Analysis

All recorded events were analyzed offline on the University of Toronto IBM 370/165 computer using essentially the same software as the online program. However, the offline program made much greater use of the calibration data mentioned in section §1.B. A description of the software is given in the next section.

An analyzed event buffer for all events with two or more charged particles was recorded on magnetic tape for further analysis of specific interactions. A breakdown of the recorded events is given in Table 4. About 28% had two oppositely charged pions; of these, about one third had two or more gamma showers.

§1.D. Reconstruction Software

The reconstruction software, as mentioned above, was essentially the same for online and offline analysis. The sequence followed in the reconstruction of an event is outlined in Figure 7. The event reconstruction program was divided into three basic sections: the beam, the charged particles, and the gamma rays.

a) Beam Reconstruction

The momentum, direction and position of the incident pion upstream of the target were determined using the information from the beam momentum hodoscope and the beam spark chambers. All multiple beam track events were rejected and

corrected for. If a beam particle fired more than one beam hodoscope element, the event was taken as having one counter set at the average position.

b) Charged Particle Momentum Determination

The first step in determining the charged particle momenta is the calculation of the particle trajectories. A considerable amount of time was saved by demanding that in each view the sparks for a track candidate fall within a road defined by the charged particle hodoscope element dimensions, an imaginary grid similar to the charged particle hodoscope at the magnet center, and the hydrogen target dimensions. Tracks were first searched for in the downstream Y view and then in the downstream X view. For the rotated chambers, cross checks were done between the two views to further constrain the track candidates. The entire procedure was repeated for the upstream chambers. At this point, the track candidates having common sparks were pruned, and the tracks with the lowest chi-squared values were kept. The upstream and downstream were next matched at the magnet center. A common intersection point of the two or more tracks with the beam track was also demanded. Analysis was aborted for events which did not have at least two such tracks. Before calculating the momentum of each charged particle, the tracks were corrected for bending outside the magnet, caused by the strong fringe field. Figure 8 shows the reconstructed trajectories for a three-pronged event.

The momenta of the surviving tracks were determined using the known corrected trajectories, in conjunction with a momentum function consisting of a fourteen-term polynomial. This momentum function was developed[3] using numerical integration of Monte Carlo generated tracks. A detailed magnetic field map was available for this purpose.

c) Gamma Shower Energy and Position Reconstruction

Events with one positive and one negative charged track were then checked for the presence of gamma showers. The reconstruction software was identical for all events, regardless of the number of gamma rays present. The procedure followed in determining the energy and position of each gamma ray shower is summarized in Figure 9. All candidates for showers were first required to have deposited an energy of at least 30 MeV in a single lead glass block. Then the gamma chambers were checked to see if, corresponding to that shower, there existed at least one X and one Y spark in either of the first two chambers, and at least

one confirming spark in a subsequent chamber. The shower center was then taken to be the position of the leading X and Y sparks, or as the average position if more than one leading spark was found. Ambiguities resulting from the overlap of charged and gamma showers were eliminated by rejecting an event if any gamma shower was found to be within 7.5 inches of an extrapolated charged particle trajectory.

The shower energy was determined by adding any energy deposited in surrounding blocks to that in the leading block, and then correcting for energy losses in the lead converter, around the photomultiplier tube, and in the junction between blocks. For all events with two or more showers (regardless of the actual number of showers), the two showers forming an effective mass closest to the π^0 mass were found and put first and second into the final analyzed event buffer in decreasing order of energy. The rest of the gammas were buffered into subsequent positions in decreasing order of energy. In Figure 10, we present the reconstruction of a two gamma shower event.

CHAPTER 2

KINEMATIC ANALYSIS

§2.A. Analysis of Four Gamma Events

Among the total number of good events, i.e., two oppositely charged pions and two or more gamma showers, 4% were found to have four gamma shower candidates. All such events were extracted and analyzed assuming the hypothesis (X = meson)

$$\pi^- p \to X n \qquad \text{(II.1)}$$

$$X \to \omega\pi^0(2)$$

$$\omega \to \gamma\gamma$$

$$\omega \to \pi^+\pi^-\pi^0(1)$$

$$\pi^0(1) \to \gamma\gamma \,.$$

We had 38000 events, each with six possible combinations, as there are six ways to form two π^0's out of four gamma rays. Our convention for the numbering of these combinations is summarized in Table 5. For each combination we also present in Table 5 the fraction of total events for which this particular combination was the "best" fit to the hypothesis II.1 (the method for determining the "best" combination is discussed in Chapter 6). Examining Table 5, one notices that 86% of the "best" combinations are either combination 1 or 6. This is due to the internal ordering introduced by the reconstruction program. The gamma ray pair forming an effective mass closest to the π^0 mass was stored in the first two buffer positions. For this reason, in the following we often plot effective masses using combination 1 only, or the sum of combinations 1 and 6. This is done simply for convenience and does not seriously bias the plots as the contribution from the other combinations is small.

Combination 1 of our initial $\pi^+\pi^-\gamma\gamma\gamma\gamma(4\gamma)$ data sample is presented in Figure 11. This is the starting point of our analysis and the only cuts applied on the data were done to avoid reconstruction problems for low momentum particles and inefficiencies of the detectors near their edges. These are cuts 1, 2, 5 and 6 of Table 6. There is a slight indication of some signal around the B(1.230) mass. Also given, in Figure 12, is the $\gamma\gamma$ effective mass from the same initial sample. This plot represents the sum of combinations 1 and 6 of $\pi^0(1)$ (or, equivalently,

the sum of combinations 6 and 1 of $_{\omega}\pi^{o}(2)$).

This data sample was then subjected to the analysis described in Figure 13, using the rest of the cuts given in Table 6. Briefly, for a combination with both gamma pair effective masses within 40 MeV of the π^{o} mass, a "2C" fit was applied. Both pairs were constrained to yield the π^{o} effective mass. Then the nucleon missing mass was calculated and combinations satisfying a cut of .5 - 1.2 GeV were "3C" fitted. The "2C" missing mass and missing mass squared are plotted in Figure 14. The "3C" fit again constrained the gamma pairs to yield the π^{o} mass, plus imposed the additional constraint of forcing the missing mass to the neutron mass. The three pion $(\pi^{+}\pi^{-}\pi^{o}(1))$ effective mass was then calculated and the combination tested for the cut $.740 \geq$ "3C" $\omega \geq .820$. The "3C" ω effective mass is plotted in Figure 15. Again only combinations 1 and 6 are used. Surviving combinations are then "4C" fitted to hypothesis II.1 yielding our final $\omega\pi^{o}$ sample. After each fit (2C, 3C and 4C), events in the lowest 5% confidence level region were rejected.

It is important to point out that often (≈50% of events) more than one combination of an event passed the above cuts. As already mentioned, the method of determining the best combination will be presented in Chapter 6. We have a total of 1781 events with at least one combination surviving all cuts; their effective mass spectrum is shown in Figure 16.

Detailed analysis of the cuts applied in our kinematic analysis, and of our final $\omega\pi^{o}$ sample, will be deferred to Chapters 5 and 6.

§2.B. Analysis of Five Gamma Events

Our sample of events with two oppositely charged pions and two or more gamma showers also contained some 4000 events (.4%) with five gamma rays. We suspected that a large part of these events might actually be four gamma events with the addition of an accidental gamma ray, which was either due to the presence of an actual uncorrelated shower or, more likely, "created" by the reconstruction software. The four gamma rays giving the best π^{o} pairs were kept and analysis proceeded exactly as explained above in §2.A.

Again detailed analysis will be deferred to Chapter 5.

CHAPTER 3
EXPERIMENTAL RESOLUTION

Detailed studies of the measurement errors were made by a previous experiment[3] using the same apparatus. These results, with minor modifications due to higher average momenta, were also valid for this experiment.

§3.A. Beam

From Table 1, the beam momentum error was

$$\frac{\Delta p}{p} = .005 \quad (\text{FWB}) . \tag{II.2}$$

The beam slope errors were very small with

$$\Delta\theta(\text{FWHM}) = ((1.3 \times 10^{-4})^2 + (.015/p)^2 t)^{\frac{1}{2}} \tag{II.3}$$

where the first term represents the angle error due to position measurement, and the second term is due to the multiple scattering of the beam in the target (t = number of radiation lengths of hydrogen seen by the beam and p is given in GeV).

§3.B. Charged Particles

The charged particle momentum error was given by

$$\frac{\Delta p}{p}(\text{FWHM}) = ((.028)^2 + (.013p)^2)^{\frac{1}{2}} . \tag{II.4}$$

The first term is due to multiple scattering of the particles in traversing the spectrometer. The second term was found by using non-interacting beam events. A momentum error of 9% (FWHM) was calculated for beam particles, corresponding to a position error of .04 inches (FWHM) for each spark. Since typical two track events had an average position error of .05 inches, the measurement error at other momenta was then approximated by extrapolating the beam measurements.

The error in the charged particle angle measurement was

(II.5) $$\Delta\theta(\text{FWHM}) = ((.0014)^2 + (.036/p)^2 t)^{\frac{1}{2}} .$$

The second term dominates the calculated error. It represents the multiple scattering in the hydrogen target. The first term was an estimate of the angle error in the position measurement.

§3.C. Gamma Showers

For symmetric π^0 decays, the fractional error in the digamma effective mass is directly proportional to that of the measured gamma energies:

$$M_{12}^2 = kE_1E_2 ,$$

$$2\frac{\partial M_{12}}{M_{12}} = \left\{ \left(\frac{\partial E_1}{E_1}\right)^2 + \left(\frac{\partial E_2}{E_2}\right)^2 \right\}^{\frac{1}{2}} .$$

Therefore for $E_1 = E_2 = E$,

$$\frac{\partial M}{M} = \frac{1}{\sqrt{2}}\frac{\partial E}{E} .$$

For these decays, plots were made of the digamma mass spectrum as a function of gamma energy. For each energy, the width of the peaks yielded the uncertainty in the energy. A fit to the correlation between the energy and its uncertainty gave

(II.6) $$\frac{\Delta E}{E}(\text{FWHM}) = .055 + \frac{.175}{\sqrt{E}} .$$

The shower position error was found by considering electrons transported through the apparatus. The positions determined by the spectrometer were compared with the positions found at the converter. The result was

(II.7) $$\Delta x(\text{FWHM}) = .3"$$

for all energies between 800 Mev and 2.5 Gev.

§3.D. Resolution Functions

An estimate of the error in the various derived quantities of a B^0 meson event is then obtained using the formulae (II.2 - II.7) to smear the appropriate quantities in conjunction with a Monte Carlo simulation program. The predicted experimental mass distributions for the π^0, ω, B^0 and neutron are given in Figure 17. The events were simulated with t-distribution as predicted by the data and with Breit-Wigner mass distributions of 10 and 125 MeV (FWHM), respectively, for the ω and B^0.

CHAPTER 4
EXPERIMENTAL ACCEPTANCE

To find the acceptance of the apparatus for the $\omega\pi^0$ reaction, we used a Monte Carlo simulation program described in Appendix A. Randomly generated events were deleted if they failed the geometric and kinematic cuts of Table 6. The program also included the statistical removal of events due to the charged pions decaying in flight, and the interactions of the pions and gamma rays in the hydrogen target. The whole process was performed for eight t-bins, with an average of 100,000 events generated for each bin. The final acceptance curve is plotted in Figure 18, and the acceptance for each t-bin is listed in Table 7.

It is important to note that the acceptance does not include an extra t-dependent correction due to the "tight" trigger mode of data collection. The stringent demands of the "tight" trigger caused losses of good events due to: (i) the rejection of an event because of a single neutron recoil setting a TA counter; (ii) the rejection of an event by the H2 requirement because of extra counts. These extra counts come from sources such as the backscatter of shower particles, the presence of delta rays, beam interactions after the hydrogen target, etc. These corrections are calculated in Chapter 7.

The average acceptance for our reaction is

$$.039 \pm .004 \ .$$

The error bounds are not indicative of statistical error (<.001), but rather are a measure of how well we understand our acceptance. Various tests of the Monte Carlo program (see Appendix A) lead us to believe that the relative error in the acceptance is 10%. This is a conservative estimate.

CHAPTER 5
SELECTION OF FINAL EVENT SAMPLE

In this chapter we will first discuss the reasons for our various cuts and the loss of good events resulting from those cuts on our data. We will then discuss the background and how we contend with it.

§5.A. Kinematic and Geometric Cuts

These cuts are summarized in Table 6. Briefly, cut 5 removed the possibility of biases due to the inefficiencies of the detectors near their edges. Cut 6 removed events in which the measured energy of a gamma shower might have been augmented by the energy of a charged pion due to the proximity of that charged pion to the gamma shower. Cuts 1, 2, 3 and 4 were applied on the data to avoid reconstruction problems for low momentum particles.

The losses due to the aforementioned cuts are corrected for in the Monte Carlo acceptance calculation presented in Chapter 4.

§5.B. Neutral Pion Mass Cut

To isolate combinations with two π^0's in the final state, a cut of 95 MeV to 175 MeV was made on both ($\gamma\gamma$) effective masses if they survived the previous cuts. The effective mass spectrum for the sum of combinations 1 and 6 is given in Figure 12 with lines indicating the cutoff region. The data was fitted to a gaussian plus a fourth order polynomial representing background[4]. We obtained a width of 24.0 ± .5 MeV (FWHM) for the π^0 peak. This is in excellent agreement with the resolution function of Figure 17. The fractional loss of good events due to the π^0 mass cuts is thus < .1% whether one uses the resolution function or the fit to the data. These very loose mass cuts were used as slightly tighter cuts did not significantly improve the signal to background ratio of the B^0 in the final $\omega\pi^0$ sample. Since we are dealing with low statistics we opted for the larger data sample.

§5.C. Missing Mass Cut

The "2C" missing mass and missing mass squared for events with two π^0's are

given in Figure 14. There is a clear neutron signal on a large background. We feel that some of the background comes from the contamination of our (B^0n) data by Δ^0's, e.g.,

$$\pi^- p \rightarrow B^0 \Delta^0(1234) \qquad \text{(II.8)}$$
$$\qquad\qquad\qquad\qquad\quad \big|_{\rightarrow n\pi^0} .$$

Results from various fits to the missing mass data lend support to our claim. The data were first fitted to a mass resolution function shape (for the neutron) plus a fourth order polynomial and then to neutron and Δ^0 mass shapes plus background (represented again by a fourth order polynomial). The latter was a 60% better fit, and produced a 285 ± 10 MeV (FWHM) neutron centered at .959 ± .002 GeV and a 390 ± 10 MeV (FWHM) Δ^0 centered at 1.250 ± .005 GeV. Folding in our resolution in the mass region concerned, we obtained a width of 135 ± 10 MeV (FWHM) for the Δ^0. We discuss the background further in §5.F.

In order to remove most of the above contamination and other sources of background, we make a .5 - 1.2 GeV mass cut on the "2C" missing mass for all events. The fractional loss of good events is estimated to be (2.4 ± 1.0) %.

§5.D. Omega Mass Cut

The "3C" three pion effective mass for those combinations with two neutral pions and a "2C" recoil mass satisfying the appropriate cuts is plotted in Figure 15. There is a clear $\omega(783)$ signal sitting on small background (the background is approximately 35% in the region defined as ω). A mass cut of 740 - 820 MeV was made to isolate combinations with an ω in their final state. As was the case for the neutral pions, we chose these limits to improve statistics. Tighter cuts did not significantly improve the final B^0 signal.

The calculation of the good event losses was done by choosing the background regions shown in Figure 15 and assuming a fourth order polynomial fit to the background between the two areas. The result was a 25.5 ± 2.5 MeV (FWHM) signal, implying a fractional loss of events of < .1%. To account for the experimental mass resolution in the ω mass region, the resonance shape was described by a Breit-Wigner function with the mass resolution folded in; the resulting fit is shown in Figure 15. The fitted values for mass and width of the ω are

(22)

$M(\omega) = 781 \pm 3$ MeV

$\Gamma(\omega) = 13.0 \pm 2.5$ MeV

in close agreement with the world average values[5].

The decay matrix element squared or Dalitz plot density

$$\lambda = \frac{|\vec{P}_{\pi^+} \times \vec{P}_{\pi^0}|^2}{\frac{3}{4}(m_{3\pi}^2/9 - m_\pi^2)^2}$$

for the three pion events within the mass cut is shown in Figure 19. The distribution is consistent with that of a $J^P = 1^-$ particle. Also plotted (Figure 20) are the dipion effective mass ($M_{\pi^+\pi^-}$) and $\mu = \hat{p} \cdot \hat{q}$, where $\hat{p}$ and $\hat{q}$ are as follows: the omega decay is analyzed in terms of a single pion plus a dipion. The pions of the dipion are assigned a momentum $\vec{q}$ (in the dipion rest frame), and the remaining pion is assigned a momentum $\vec{p}$ in the ω rest frame. The results are consistent with that expected for the ω[6].

§5.E. Summary of Good Event Losses

Since we are calculating the cross section for

(II.9)

$$\pi^- p \to B^0 n$$
$$\quad \downarrow \omega\pi^0$$
$$\quad\quad \downarrow \text{all}$$

we must correct for unseen ω decay modes. This correction factor is simply $.899 \pm .006$[5].

The above factor and all mass cuts are listed in Table 8 along with the calculated event loss fractions. The net correction factor was calculated to be $.67 \pm .09$. This factor will be used in the differential cross section calculations.

§5.F. Background

As already mentioned earlier, we feel that some of our ($B^0 n$) data is actually

(II.10)

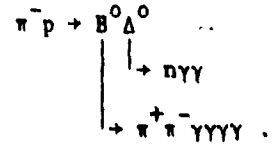

The contamination is expected to be minimal for data taken under "tight" trigger conditions (one or more TA veto event). However, under "loose" trigger requirements (two or more TA required to veto event), Monte Carlo simulations show that the acceptance for ($\pi^- p \to B^0\Delta^0$) is approximately 50% that of ($\pi^- p \to B^0 n$). We took 20% of our data with a "loose" trigger. A cut of 1.2 GeV on the missing mass removes some of this background but a Δ^0 fit to the missing mass shows that 38% remains under the neutron peak. This is taken into account by using a $B^0\Delta^0$ type reflection as part of the background of the "4C" $\omega\pi^0$ sample. That is, events were simulated with a Δ^0 mass distribution (mass < 1.2 GeV) and then "4C" fitted to give the required $\omega\pi^0$ distribution.

Another source of background that we investigated was the reaction

(II.11)

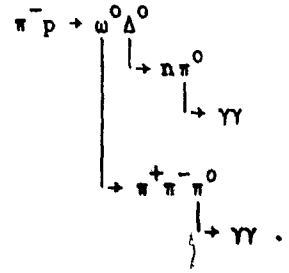

However, our apparatus has no acceptance for this reaction, the neutral pion (from the Δ^0 decay) being too "soft". Our data confirms this, as effective mass plots of $n\pi^0$ combinations show no signal at the Δ^0 mass.

We also considered the 4000 5γ events and the possibility that these events, or some part thereof, might actually be 4γ events with the addition of a fictional gamma ray. Therefore, the 5γ data was analyzed as detailed in Chapter 2 and the results were as follows: only 26 events survived all cuts and their $\omega\pi^0$ effective mass plot had no significant enhancement anywhere. Moreover none of these events had a missing mass within 100 MeV of the neutron mass, implying a very poor fit to the hypothesis

(II.12)

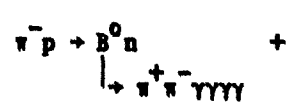

It would appear that almost none of the 5γ events were of the type II.12.

CHAPTER 6
FINAL B^0 SAMPLE

In Figure 16, the mass distribution $M(\omega\pi^0)$ is given for the 1781 events with $M(\pi^+\pi^-\pi^0(1))$ in the ω region and both $M(\gamma\gamma)$ in the π^0 region. As explained in Chapter 2, there are six possible B^0 combinations for each event. Whenever two or more combinations survived all cuts, the "best" B^0 combination was chosen to be the one with the largest ω decay matrix element. It is the effective mass of these B^0's that has been plotted in Figure 16. The predominant feature is the strong B^0 signal. We have 840 events in the B^0 region, defined as

$$M(\omega\pi^0) = 1.155 - 1.305 \text{ GeV} .$$

No anomaly in the ω Dalitz plot is found[16] and the B^0 signal appears strongly with ω's located at the center as well as at the periphery of the Dalitz plot. A good fit is obtained (full curve) by assuming a linear combination of a Breit-Wigner resonance shape for the B meson (with resolution at the B mass folded in), reflection from the state $B^0\Delta^0$, and the Monte Carlo generated phase space for $\omega\pi^0 n$. The resulting fit is shown in Figure 16. We obtained

$$M(B^0) = 1.232 \pm .008 \text{ GeV}$$
$$\Gamma(B^0) = 147 \pm 20 \text{ MeV}$$
$$\text{and } \chi^2 \text{ (67 degrees of freedom)} = 78 .$$

The fraction of good events lost due to the B^0 mass cuts is $(.23 \pm .05)$.

We remark that the apparent disagreement between the width of our observed signal and published data[5] is, we believe, due to the poor statistics. We have already shown, by our calculation of the π^0 and ω resolution functions, that our errors are reasonably well understood.

We present angular decay distributions although, owing to low statistics, the results are far from conclusive. In our analysis, we used the following convention: θ and ϕ are the polar and azimuthal angles, respectively, of the $\omega(\vec{p}_\omega)$ in the B rest frame. A right-handed coordinate system is chosen so that the z-axis is along the B direction in the overall C.M. system, i.e., helicity (H) frame; y is normal to the production plane, $\vec{y} = (\vec{\pi}_{in} \times \vec{B})$; χ and ψ are the polar and azimuthal angles, respectively, of the normal to the ω decay plane in

the ω rest frame, measured in a system x', y', z', where $\vec{z}' = \vec{p}_\omega$ and $\vec{y}' = \vec{z} \times \vec{z}'$ (in the B rest frame). See Figure 21.

In Figure 22, we plot the distributions of $\cos\theta$ and ϕ. The upper histograms include all events in the B region (Figure 16). The lower histograms are plotted after subtracting the background distributions of the control regions A and C (Figure 16), defined between .96 - 1.06 and 1.4 - 1.5 GeV, respectively, with weights according to the fitted values of B^0 and background in the B region. Both upper and lower histograms are corrected for acceptance.

The subtracted distributions are almost symmetric (within errors) as expected for a well defined J^P state (tightening the π^0 and ω mass cuts does not significantly change the distributions). The results are far from conclusive and a larger sample is needed before any meaningful angular analysis can be performed. We are currently analyzing data obtained in subsequent experiments[7,8] and expect to increase our B^0 sample fivefold. In Figure 23, we present the $\cos\chi$ and ϕ distributions.

CHAPTER 7
INEFFICIENCY CORRECTIONS

In calculating our cross section we must correct for inefficiencies of the apparatus and of the reconstruction software. We discuss these corrections below and summarize the information in Table 9.

§7.A. Gamma Ray Conversions Upstream of the Lead Converter

The loss of events due to gamma rays converting inside the hydrogen target was included in the acceptance calculation. That loss due to conversion along the trajectories towards the converter was calculated independently. The loss was determined by calculating the amount of material traversed by the gamma rays. The greatest contributors to this effect are the spectrometer chambers (aluminum and mylar sheets). From their known collision lengths, the probability of conversion for 2γ events was calculated to be $(9.8 \pm .9)\%$ [3]. Therefore, for 4γ events, it is simply $(18.7 \pm 1.1)\%$.

§7.B. Event Rejections by Gamma Hodoscope Trigger

In Part I, we saw that an event trigger occured only if at least two NO-YES combinations were found in the paired gamma hodoscope. This requirement was a potential source of bias because charged particles from the ω decay and backscatters from the lead glass were also seen by GHR. We expected this effect to be quite small as we require four NO-YES combinations. We investigated this problem with data taken with a weaker gamma trigger requiring only one NO-YES pair (~22% of data). No losses whatsoever were found.

§7.C. Conversion Efficiency of Lead Converter

The gamma conversion efficiency is highly dependent on the effective cutoff energy for observed secondary electrons. However, this cutoff energy is very difficult to measure since it is dependent on the position of the conversion in the lead, and the energy and emission angle of the electron. Therefore, the value for the single gamma efficiency was taken as the average between an upper limit based on pair production predictions, and a lower limit from published Monte Carlo

results.

The upper limit was obtained by using the theoretical pair production cross section limiting value of $7/9$[2] to scale the thickness of our lead converter (1.6 RL), yielding a conversion efficiency of 71.2%.

The lower limit was obtained from published Monte Carlo results for photon showers by Messel and Crawford[9]. The secondary cutoff energy for our detector lies somewhere below 10 MeV[3]. From the shower tables a value of 62.9% is predicted for a 10 MeV cutoff. We believe the parameters of our system lie between the two extremes. Therefore the average was taken, (67.1 ± 4.5)%, with a systematic error covering the two limits. By raising this result to the fourth power, we obtain the 4γ efficiency, (.203 ± .021).

§7.D. Gamma Software Reconstruction Failure

The software reconstruction inefficiency was measured by hand-scanning 1000 2γ events on a CRT display by means of an interactive program that permitted operator determination of gamma showers. The result for the 2γ events was an inefficiency of (2 ± 2)%. For 4γ events, the inefficiency is simply (4.0 ± 2.8)%.

§7.E. Digitization Scaler Runout

We studied the possibility of losing a real gamma shower due to an insufficient number of scalers. We expected this effect to be substantial since a study of 3γ events showed a (.70 ± .03)% loss[10]. The method employed is quite simple. The spark positions for each X and Y plane were read, starting at the positive X and positive Y ends, respectively. Therefore, a scaler runout would result in a depletion of the negative X and Y positions, in contrast to the expected symmetry about the origin in the normal 100% efficient case. We studied only the Y plane, as the X plane is not expected to be symmetric due to the 2.5 degree angle between the spectrometer Z-axis and the target Z-axis. We plotted the Y position of 155,000 showers and determined that there was a depletion of 6650 showers in the negative Y region. If we attribute this depletion completely to scaler runout, there is a loss of (4.3 ± .4)% per plane. Therefore, the total loss due to scaler runout is (8.4 ± .6)%.

§7.F. Partial Gamma Detector Inefficiency

This is a time dependent correction that was handled by the reconstruction software. The participation of each gamma chamber plane in each event was continuously monitored and recorded. At the end of a run, the efficiency of each chamber and the single gamma efficiency were calculated from the individual participation ratios using the procedure described in Appendix B. However, these figures were calculated for 2γ events only, since the largest fraction of our data was 2γ events.

For 4γ events, the efficiency is expected to be lower because the same charge is distributed among more sparks. Separate single gamma efficiencies for events with three or more gammas were not calculated by the software. We studied this problem and determined the efficiency for the final $\omega\pi^0$ event sample of Figure 16 using the same method described in Appendix B. The single gamma efficiency for these events was (.974 ± .010). Therefore, the net efficiency for the $\omega\pi^0$ events was (.900 ± .018). The single gamma efficiency for all 2γ events (.986 ± .002) is already taken into account in the effective beam flux (a factor of .972 ± .004 for two gammas), and thus, the effective correction factor to be used is (.930 ± .018).

§7.G. Partial Charged Spectrometer Inefficiency

Again this is a time dependent correction which was handled by the reconstruction software. This factor was taken into account in the calculation of effective beam.

§7.H. Beam Contamination

The muon content in the beam was found to be (2.0 ± .6)% at 8.45 GeV/c by measuring the amount of beam that traversed three feet of steel. Kaon contamination was estimated at .6% (published yield curves[11]) and electron contamination should be negligible (severe phase space restrictions).

§7.I. Charged Pion Interaction in Detector

From the known cross sections of mylar, aluminum etc., an attenuation of

(2 ± 1)% is determined for an incident pion. Thus, the probability of losing one or both pions is (4.0 ± 1.4)%.

§7.J. Tight Trigger Losses

As mentioned in Part I, most of our data was collected under a "tight" trigger mode which demanded that two or three H2 scintillator elements be hit and no TA elements be set. To permit offline investigation of the effects of these constraints, we collected ~18% of our data under a "loose" trigger which demanded H2 > 1 and allowed one TA to be set. Subsequent investigations showed that our tight H2 constraints caused an (8.1 ± .5)% loss, and tightening our TA requirements caused a further (15.6 ± 1.4)% loss. Investigation of other reactions by members of our collaboration have shown the TA loss to be t-dependent[12]. However, owing to our poor statistics, we use a constant correction with systematic error covering all t-dependent fluctuations.

The product of these two factors with a dilution factor (to account for the fact that only some data was taken under a tight trigger) gives us our final effective correction of (.800 ± .014).

§7.K. Miscellaneous Corrections

Losses due to scintillation counter inefficiencies (cracks, etc.) were calculated to be (3.2 ± .8)%. This was determined by interactive scanning of 1000 events on a CRT. The target was surrounded by a ¼-inch layer of polyethylene to stop low energy particles. Therefore, we can ignore losses due to δ ray creation inside the target.

§7.L. Summary

The event loss fractions caused by the inefficiencies described in this chapter are listed in Table 9. The final overall correction factor is .098 ± .010.

CHAPTER 8

THE $B^0 \rightarrow \omega\pi^0$ DIFFERENTIAL CROSS SECTION

The differential cross section was calculated using the following expression -

$$\frac{d\sigma}{dt'} = \frac{Y(t') \times 10^{30}}{\beta \times N \times \epsilon \times \Delta t' \times A(t')} \quad ub/(GeV/c)^2 \qquad (II.13)$$

where

$Y(t')$ = yield of good events in each t' bin

β = total effective beam flux

N = number of protons in the hydrogen target / cm^2

ϵ = constant corrections

$\Delta t'$ = t' interval ($t' = t - t_{min}$, where the average t_{min} at our energy is ~.009 GeV^2)

$A(t')$ = acceptance in each t' bin .

The constant correction factor (ϵ) is the product of the correction factor due to mass cuts (Table 8) and that due to inefficiency corrections (Table 9). We correct the total beam flux for spectrometer and gamma chamber inefficiencies, and for losses due to the presence of dual beam tracks in certain events (~12%). The result is the effective beam flux, and it is this number (β) we use in the $d\sigma/dt'$ calculations.

The differential cross section for reaction II.9 is presented in Figure 25 and listed in Table 10. The error bars are only statistical errors and do not include an overall normalization (systematic) error of 19%. The integrated cross section is 11.0 ± 2.1 μb. This distribution was obtained by fitting the $\omega\pi^0$ mass plots at various t' slices, but with fixed mass and width values for the B^0 as obtained from the total fit. The background subtractions for the smaller t bins used for the differential cross section were obtained by interpolating between these fitted points. The fractions of good events per t' bin, as determined by the above fits, are summarized in Table 11.

CONCLUSIONS

We have described the investigation of the decay

$$B \to \omega\pi^0$$
$$\quad\;\; \lfloor\!\to \pi^+\pi^-\pi^0$$

and calculated the differential cross section. The mass and width of the B^0 are in reasonable agreement with the published data on the charged B.

The B^0 differential cross section is quite broad and shows no forward turnover. Several papers[17,18] have proposed A_2 exchange as the most important mechanism in B^0 production. A_2 exchange, which couples mainly to helicity flip at the nucleon vertex, should[17] produce a forward turnover in the differential cross section. The lack of a forward turnover and a small integrated cross section indicate that A_2 exchange does not play a strong role in B^0 production. A similar conclusion has been reached from analysis[19] of charged B production.

As already noted we are currently analyzing data obtained in subsequent experiments[7,8] and expect to increase our statistics at least fivefold. This will permit the angular analysis of the B^0 decay products and the determination of the B^0 density matrix elements. This will, in turn, allow us to greatly reduce the error in our acceptance calculation, which is due to the presently unknown distribution of B^0 helicities. The uncertainty in acceptance is currently one of our largest systematic errors.

Assuming that what we are seeing is indeed the B^0 ($J^P = 1^+$), the determination that ρ_{00} is large (implying natural parity exchange), together with the lack of a forward turnover, would be very troublesome as we know of no $I = 1$ natural parity exchanges with large helicity non-flip couplings.

APPENDIX A

ACCEPTANCE CALCULATION

The cross section had to be corrected for losses due to:

a) the geometry of the detection and triggering apparatus,

b) the triggering constraints, and

c) the geometric and kinematic constraints of Table 6.

This correction was done using a Monte Carlo simulation program producing events of the form

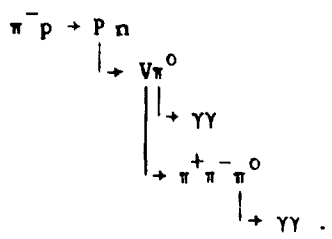

Each event was described by four kinematic quantities: the beam momentum, the four-momentum transfer squared, the $(V\pi^0)$ effective mass, and the $(\pi^+\pi^-\pi^0)$ effective mass. We applied the program to our particular decay, $P \to B^0$ and $V \to \omega$, and calculated the acceptance as a function of t. The B^0 and ω masses were generated randomly with Breit-Wigner distributions of width and mass as given in reference (5).

The generation of events went as follows: the B^0 was made to decay to $\omega\pi^0$ in the B^0 rest frame. A right-handed coordinate system was chosen so that the z-axis was along the B^0 direction in the overall C.M. system, i.e., Helicity frame; y was chosen normal to the production plane, $\vec{y} = (\vec{\pi}_{in} \times \vec{B})$. The B^0 mass uniquely determines $|\vec{P}_\omega| = |\vec{P}_{\pi^0}|$ and a choice of ϕ_ω and $(\cos\theta)_\omega$ completely specify the four momenta of the ω and π^0. We assumed that the $B^0 \to \omega\pi^0$ decay is uniquely S-wave and thus $\cos\theta$ and ϕ were randomly chosen. This is somewhat incorrect as the intensity of the D-wave has been found to be 4-9%[13,14] that of the S-wave. This error was taken into account in the overall error calculation.

Next we considered the ω decay. There are five independent kinematic variables (neglecting spin) needed to describe the 3π decay of the ω. Three variables are needed to describe the orientation of the decay plane (ω rest frame) in space.

The decay plane is then parametrized by two more variables. We chose the dipion effective mass, $M_{\pi^+\pi^-}$, and $\hat{p}\cdot\hat{q} = \cos\theta = \mu$:

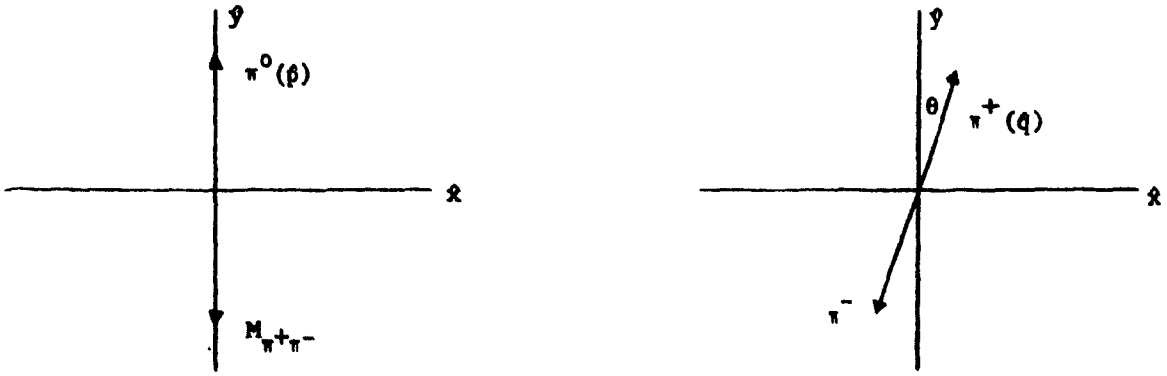

The distribution for these two variables in the decay of a $J^P = 1^-$ particle is given by (6,15):

$$\frac{dN}{dM_{\pi^+\pi^-}} = (F(M_\omega, M_{\pi^+\pi^-}, M_{\pi^0})^3 \times F(M_{\pi^+\pi^-}, M_{\pi^+}, M_{\pi^-})^3)$$

$$= p^3 q^3$$

and

$$\frac{dN}{d\mu} = (1 - \mu^2)$$

where

$$F(x,y,z) = \frac{(x^2 - (y+z)^2)^{1/2}(x^2 - (y-z)^2)^{1/2}}{2x} .$$

We now consider the orientation of the 3π decay plane. The ω was made to decay in the ω helicity rest-frame; i.e., the ω direction was chosen as the z-axis, and the y-axis was chosen along $\vec{z}' \times \vec{z}$ in the B^0 rest frame (z' is the z of the B^0 helicity frame described earlier). Lacking density matrix information, we assumed uniform distributions for the three angles describing the decay plane in space. To obtain an estimate of the error involved in making such an assumption,

we calculated the acceptance as a function of $\cos\theta'$, where θ' is the angle between the z-axis (beam direction) and the normal to the ω decay plane in the lab. Our error was estimated at being less than 8%.

After a complete event was generated, it was rotated to an arbitrarily chosen production plane and transformed to the laboratory frame. The production plane was then randomly rotated about z (the beam direction) and the π^0's allowed to decay uniformly in their respective rest frames. The geometric and kinematic constraints of Table 6 were applied, and events failing the cuts were deleted. Then the two following trigger constraints were checked:

a) the presence of at least one charged particle outside the one inch hole in the HØ counter;

b) a unique H2 hodoscope element for each charged particle.

Events were also rejected statistically to account for decays of the charged pions in flight, and interactions and conversions of the particles in the hydrogen target:

a) Charged Pion Decay in Flight

$$\text{Probability of decay} = \frac{(\text{distance in inches from target to last chamber})}{\beta\times(307.2)}$$

b) π^+,π^- Interactions in Target

Probability of interaction = (path length in hydrogen target in inches)×.00325, assuming an interaction cross-section of 30 mb.

c) Conversion of Gammas in Target

Probability of conversion = (path length in hydrogen in inches)×.00198, assuming a scaling of the thickness by .69.

The final acceptance was the fraction surviving all the cuts and deletions. As a check on our understanding of the acceptance, we plotted the magnitude of the momentum of various particles; first, as predicted by Monte Carlo simulation, and then as obtained from our data (see Figure 24). We have good agreement in

all cases.

Our acceptance is tabulated as a function of t', in Table 7, and plotted in Figure 18.

The acceptance as a function of $\cos\theta$, $\cos\psi$, ϕ and ψ was also calculated so as to correct angular distribution plots. θ and ϕ are the polar and azimuthal angles, respectively, of the $\vec{\omega}$ in the B^0 rest frame, with x, y, and z as in the B^0 helicity frame; ψ and ϕ are the polar angle and azimuthal angle of the normal to the omega decay plane in the ω helicity rest frame.

APPENDIX B

GAMMA SHOWER CHAMBER EFFICIENCY CALCULATION

In the gamma system there were two views - plane x and elevation y - each having three planes. We label the three x planes 1, 2 and 3, and the three y planes 4, 5 and 6. A shower was accepted if one view had at least two planes firing, and the other view had at least one plane firing.

We make the following definitions:

ε_i = efficiency of chamber plane i

$$= \frac{\text{number of times the plane contained a spark}}{\text{number of tracks through the chamber}}$$

P_i = participation ratio of plane i for a found event

$$= \frac{\text{number of times the plane fired in a found event}}{\text{number of found events}}$$

Then the probability $P(\geq 2)$ of at least two of the three planes in one view firing is given by

(B.1) $$P(\geq 2) = \varepsilon_i\varepsilon_j(1-\varepsilon_k) + \varepsilon_i(1-\varepsilon_j)\varepsilon_k + (1-\varepsilon_i)\varepsilon_j\varepsilon_k + \varepsilon_i\varepsilon_j\varepsilon_k$$

$$= \varepsilon_i\varepsilon_j + \varepsilon_i\varepsilon_k + \varepsilon_j\varepsilon_k - 2\varepsilon_i\varepsilon_j\varepsilon_k \ , \quad (i,j,k) = (1,2,3) \text{ or } (4,5,6).$$

Therefore the probability P_γ of finding a shower, when one is present, can easily be found to be

(B.2) $$P_\gamma = P_x(\geq 2) \times P_y(\geq 2)$$

$$+ P_x(\geq 2) \times (\varepsilon_4(1-\varepsilon_5)(1-\varepsilon_6) + \varepsilon_5(1-\varepsilon_4)(1-\varepsilon_6))$$

$$+ P_y(\geq 2) \times (\varepsilon_1(1-\varepsilon_2)(1-\varepsilon_3) + \varepsilon_2(1-\varepsilon_1)(1-\varepsilon_3)) \ .$$

We can now write expressions for the participation ratios, using the definition for P_i and the expressions (B.1) and (B.2). For the x view,

$$\text{(B.3)} \qquad \frac{P_1}{\varepsilon_1} = \frac{P_y(\geq 2) + (\varepsilon_2+\varepsilon_3-\varepsilon_2\varepsilon_3) \times (\varepsilon_4(1-\varepsilon_5)(1-\varepsilon_6) + \varepsilon_5(1-\varepsilon_4)(1-\varepsilon_6))}{P_\gamma}$$

$$\text{(B.4)} \qquad \frac{P_2}{\varepsilon_2} = \frac{P_y(\geq 2) + (\varepsilon_1+\varepsilon_3-\varepsilon_1\varepsilon_3) \times (\varepsilon_4(1-\varepsilon_5)(1-\varepsilon_6) + \varepsilon_5(1-\varepsilon_4)(1-\varepsilon_6))}{P_\gamma}$$

$$\text{(B.5)} \qquad \frac{P_3}{\varepsilon_3} = \frac{P_y(\geq 2) \times (\varepsilon_1+\varepsilon_2-\varepsilon_1\varepsilon_2)}{P_\gamma} \quad .$$

Identical expressions hold for the planes of the second view under the exchange $(1,2,3) \leftrightarrow (4,5,6)$.

To calculate the single shower efficiency P_γ, we needed the efficiencies ε_i, given the P_i from the recorded data. This was done by solving for ε_i in (B.2) to (B.5) using an iterative procedure. The starting values for ε_i on the right-hand-side of (B.3) - (B.5) were taken as the P_i. A new set of ε_i were found and the process was repeated until stable results were reached, usually after only a few iterations. The single shower efficiency was obtained by substituting these final chamber efficiencies into (B.2), and the four gamma shower efficiencies easily followed.

REFERENCES

1. ZGS Experiment No. 397, Argonne National Laboratory (October 1975, December 1975 and April 1976).

2. B. Rossi, *High Energy Particles*, Prentice-Hall (1952) 81-83.

3. M.H. Shaevitz, "A high statistics study of ω^o production at 6.0 Gev/c", Ph.D. Thesis, The Ohio State University (1975).

4. CERN/MINUIT, version 5.75 was used for all fitting.

5. Particle Data Group, "Review of particle properties", *Rev. of Modern Physics* 48 N.2 (1976) Part II.

6. M.L. Stevenson et al., *Phys. Rev.* 125 N.2 (1962) 687.

7. ZGS Experiment No. 420, Argonne National Laboratory (December 1976, January 1977 and March 1977).

8. ZGS Experiment No. 428, Argonne National Laboratory (June 1977 and July 1977).

9. H. Messel and D.F. Crawford, *Electron-Photon Shower Distribution Function Tables for Lead, Copper, and Air Absorber*, Pergamon Press (1970).

10. C.J. Zanfino, "Experimental investigation of the radiative decay $\eta' \to \omega\gamma$", M.Sc. Thesis, McGill University (1976).

11. *ZGS User Handbook*, Argonne National Laboratory (1974).

12. N.R. Stanton, private communication, The Ohio State University.

13. S.U. Chung et al., *Phys. Rev.* 11D N.9 (1975) 2426.

14. V.Chaloupka et al., *Phys. Lett.* 51B N.4 (1974) 407.

15. R. Hagedorn, *Relativistic Kinematics*, Benjamin (1964) 112.

16. G. Goldhaber et al., *Phys. Rev. Lett.* 15 (1965) 118; S.U. Chung et al., *Phys. Rev.* 165 (1968) 1491.

17. G.C. Fox and A.J.C. Hey, *Nucl. Phys.* B56 (1973) 386.

18. A.C. Irving and V. Chaloupka, *Nucl. Phys.* B89 (1975) 345.

19. U. Karshon et al., *Phys. Rev.* D10 (1974) 3608.

TABLES

TABLE 1

E-397 BEAM CHARACTERISTICS

Momentum -	8.45 GeV/c
Beam Spill -	600 msec (FWHM)
Final Focus Spot Size -	½" × ½"
Flux -	6×10^4 pions per pulse
Production Angle -	1.5°
Momentum Bite -	2½ %
$\Delta P/P$ -	.005
Beam Spark Chamber -	Spacing = 36" Position resolution Δx = .02" FWHM
Beam Direction Measurement -	$\Delta\theta$ = .0002 $\Delta x_{intercept}$ = .030"
Focus -	120" downstream of hydrogen target
Hydrogen Target -	2" diameter × 16" length

TABLE 2

SPECTROMETER CHARACTERISTICS

Spark Chambers -	Rotation	Active Area	Distance from Target
Upstream - 1	0^{o}	24" × 16"	19.00"
2	45^{o}	28" × 18"	24.50"
3	0^{o}	40" × 30"	29.75"
4	45^{o}	42" × 36"	35.00"
5	0^{o}	40" × 40"	40.50"
Downstream - 1	15^{o}	5' × 7'	91.50"
2	15^{o}	5' × 7'	97.50"
3	0^{o}	5' × 7'	103.50"
4	0^{o}	5' × 7'	109.50"
5	0^{o}	5' × 7'	115.50"

Magnet -

Type	picture frame SCM-104
Nominal $\int B \cdot dl$	240 kg-inches
Central Field	5.9 kgauss
Size	84" W × 40" H × 40" D
Center	63" from LH_2 target

Chamber High Voltage -

Method	capacitor bank discharge
Capacitance	10 nfarads / 5' × 7' area
Pulse Height	6.8 KV
Risetime	150 nsec
Delay	550 nsec
Clearing Field	75 V DC
Pulsed Field	1 KV - 600 nsec

Readout -

Method	magnetostrictive
System	SAC Midas, 4 scalers/plane

continued....

TABLE 2

SPECTROMETER CHARACTERISTICS (continued)

Resolution -

Position	.05" (FWHM)
Momentum	4% (FWHM) at 2 GeV/c

TABLE 3

SCINTILLATION COUNTERS

Name	Size	Position (Z downstream, Z=0 at LH_2 target)	Purpose
S1	1/16" × 2" × 1½"	-	
B1	1/8" × 3" × 3"	-170.0"	Detect beam
B2	1/16" × 2" × 2"	- 36.0"	
BHR BHL	½" × 16" × 24", with 1" hole	- 25.0"	Anti beam halo
HØ	1/8" × 17" × 24", with 2" hole	+ 14.0"	Signals a charged particle at an angle to the beam > 4^{o}
AA1	opening 26" × 16"	+ 23.0"	Anti particles outside fiducial volume
AA2	opening 40" × 40"	+ 42.0"	
H2	30 counters, each 1/8" × 4" × 42"	+122.8"	Charged particle hodoscope
BV1	½" × 4" × 4"	+124.0"	Veto non-interacting beam
BV2		+129.0"	
CHF	16 counters, each	+140.0"	No gamma hodoscope
CHR	½" × 7½" × 30"	+143.5"	Yes
Target anti-counters	4 alternate layers of 1/8" scintillator and ½" lead sheets placed each side of target		Veto particles at wide angles from the target

TABLE 4

BREAKDOWN OF RECORDED EVENTS

Type	Percentage (%)
Calibration events	4.0
Double beam events	12.0
Single prong, three prong, or two prong same charge events	56.5
Good two prong events:	27.5
less than two gamma showers	17.6
two or more gamma showers:	9.9
two gamma showers	7.6
three gamma showers	1.9
four gamma showers	.4

TABLE 5

COMBINATION NUMBERING CONVENTION

Combination	$\pi^0(1)$	$\pi^0(2)$	"Best" Fraction
1	$\gamma_1\gamma_2$	$\gamma_3\gamma_4$	.417
2	$\gamma_1\gamma_3$	$\gamma_2\gamma_4$	.041
3	$\gamma_1\gamma_4$	$\gamma_2\gamma_3$	.078
4	$\gamma_2\gamma_3$	$\gamma_1\gamma_4$	.014
5	$\gamma_2\gamma_4$	$\gamma_1\gamma_3$	.047
6	$\gamma_3\gamma_4$	$\gamma_1\gamma_2$	.444

NOTE: The subscript on the γ refers to its position in the event buffer.

TABLE 6

GEOMETRIC AND KINEMATIC CUTS

Energy and Momentum Cuts

1)	Charged particle momenta	> .4 GeV/c
2)	Gamma ray energies	> .2 GeV/c
3)	Two gamma rays forming π^0(1): ratio $\frac{\text{slow gamma energy}}{\text{fast gamma energy}}$	> .11
4)	Two gamma rays forming π^0(2): ratio $\frac{\text{slow gamma energy}}{\text{fast gamma energy}}$	> .085

Geometry Cuts

5) All charged and gamma ray trajectories within the detectors by 1".

6) Gamma ray to charged particle distance at lead convertor > 7.5".

TABLE 7

EXPERIMENTAL ACCEPTANCE

$-t'$	Acceptance
.00 - .01	.048
.01 - .03	.047
.03 - .05	.047
.05 - .10	.045
.10 - .20	.041
.20 - .30	.036
.30 - .40	.031
.40 - 1.00	.023

TABLE 8

MASS CUT CORRECTIONS

Mass of $(\gamma\gamma)_1$ = 135 ± 40 MeV	< .001
Mass of $(\gamma\gamma)_2$ = 135 ± 40 MeV	< .001
Mass of $(\pi^+\pi^-\pi^0(1))$ = 780 ± 40 MeV	< .001
Mass of $(\omega\pi^0(2))$ = 1.230 ± .075 GeV	.230 ± .090
Mass (recoil) between .5 and 1.2 GeV	.024 ± .010
ω unseen decays	.101 ± .006

CORRECTION FACTOR = .67 ± .09

TABLE 9

INEFFICIENCY CORRECTIONS

Correction	Fraction Loss
Gamma ray conversion upstream of lead converter	.187 ± .011
Gamma hodoscope rejection of good event	no losses
Conversion inefficiency of lead converter	.797 ± .021
Gamma software reconstruction failure	.040 ± .028
Digitization scaler runout	.084 ± .006
Gamma partial chamber inefficiency	.070 ± .018
Beam contamination	.026 ± .006
Charged pion interaction in detector	.040 ± .014
Counter inefficiency	.032 ± .008
Tight trigger losses	.020 ± .014

CORRECTION FACTOR = .098 ± .010

TABLE 10

$B^0 \rightarrow \omega\pi^0$ DIFFERENTIAL CROSS SECTION

t' Bin	Δt'	Y(t')	A(t')	dσ/dt (μb/GeV^2)	Statistical Error
.00 - .02	.02	49.1	.048	40.4	± 3.9
.02 - .05	.03	69.5	.047	38.9	± 3.4
.05 - .10	.05	96.2	.045	32.7	± 2.6
.10 - .20	.10	146.5	.041	27.1	± 1.7
.20 - .30	.10	107.7	.036	22.7	± 1.7
.30 - .40	.10	45.7	.031	11.2	± 1.1
.40 - .60	.20	42.4	.026	6.4	± .6

TABLE 11

GOOD EVENT PERCENTAGES

t' Range	Fraction of Good Events
.00 - .03	.64 ± .05
.03 - .10	.75 ± .05
.10 - .30	.73 ± .05
.30 - 1.00	.58 ± .05

FIGURES

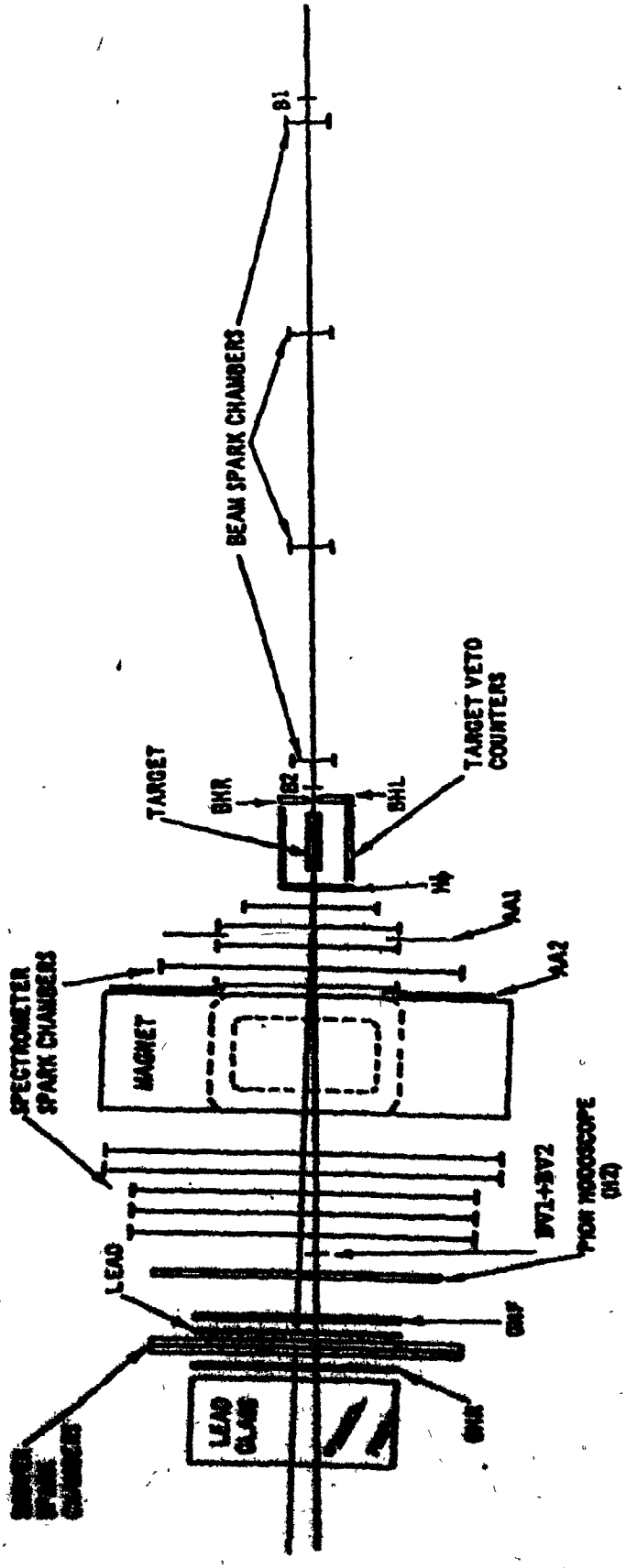

FIGURE 1 Experimental Layout

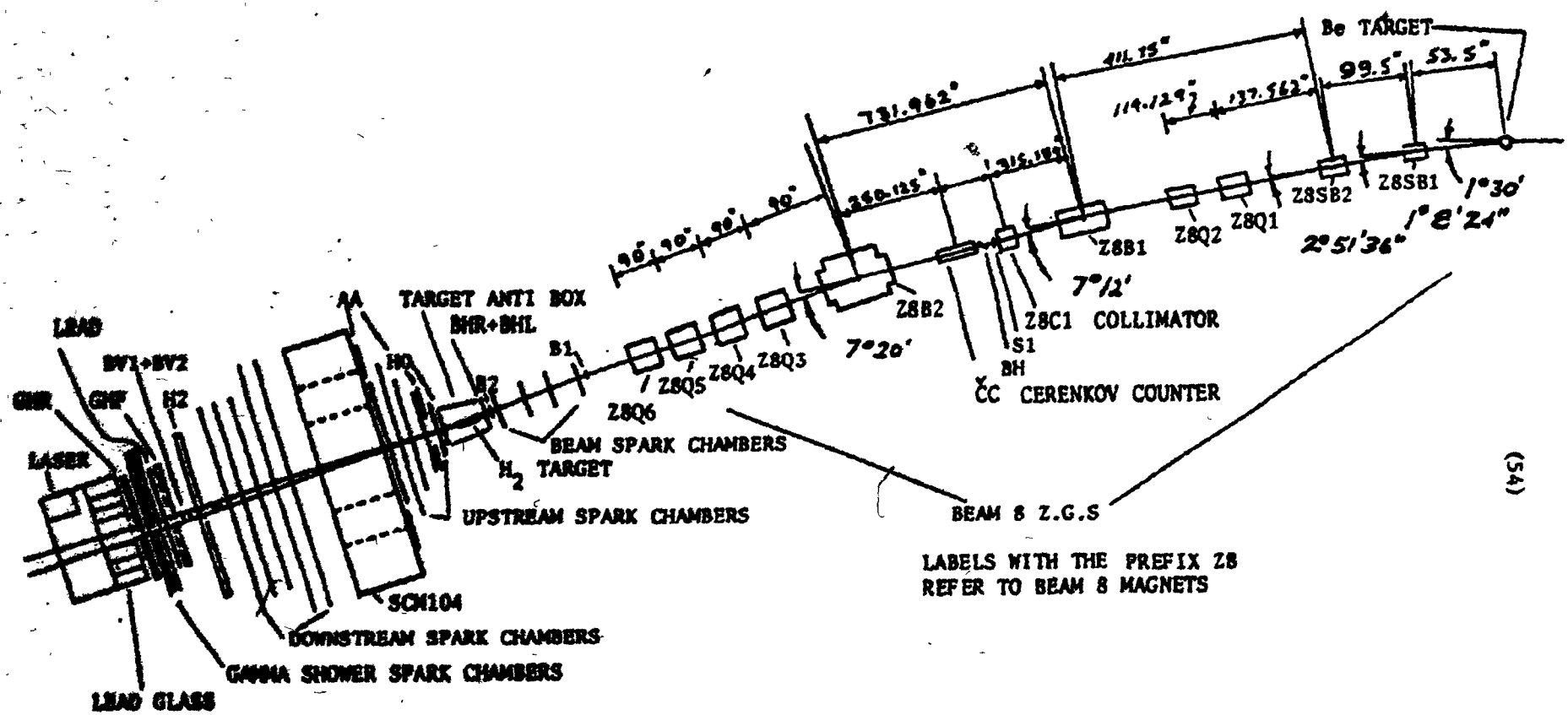

FIGURE 2 Beam Layout

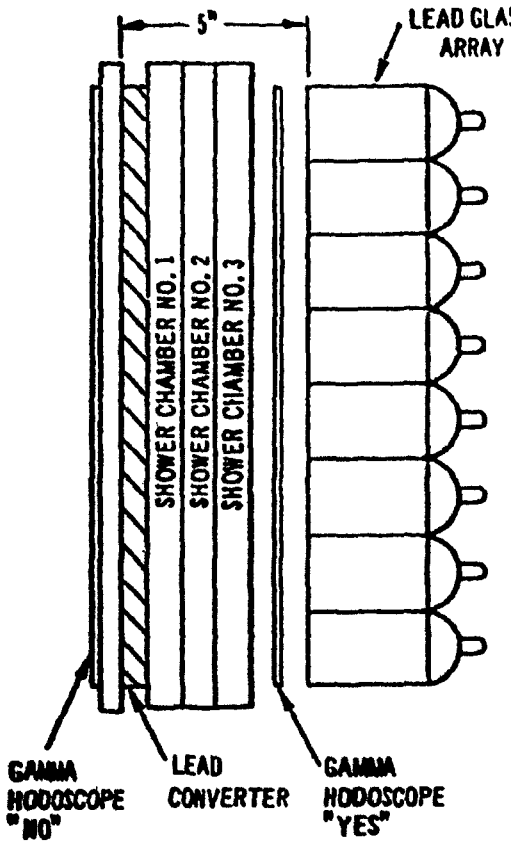

SHOWER SPARK CHAMBERS

ROTATED	ACTIVE AREA	DISTANCE FROM CONVERTER
NO. 1 - NO	5' x 5'	0.5"
NO. 2 - 12.5°	5' x 5'	1.5"
NO. 3 - 12.5°	5' x 5'	2.5"

LEAD CONVERTER

1.6 R.L. x 60" x 60"

POSITION:

140" DOWNSTREAM OF HYDROGEN TARGET

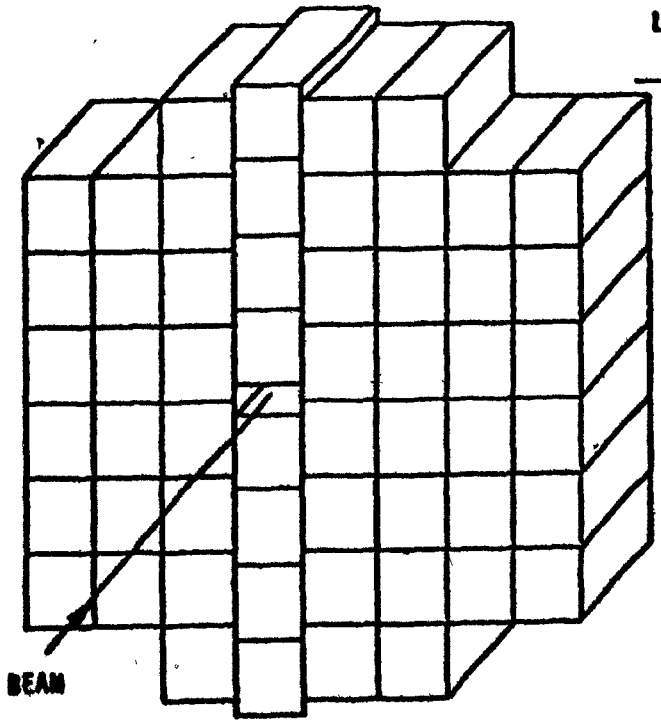

LEAD GLASS CERENKOV COUNTER ARRAY

SIZE: 7-1/2" x 7-1/2" x 12"

TYPE OF GLASS BOURNS OPTICAL PEM 62

PHOTOTUBE (5" D) EMI

GLUED DIRECTLY TO BLOCK

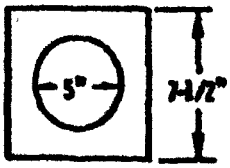

FIGURE 3 Lead Glass Gamma Detector

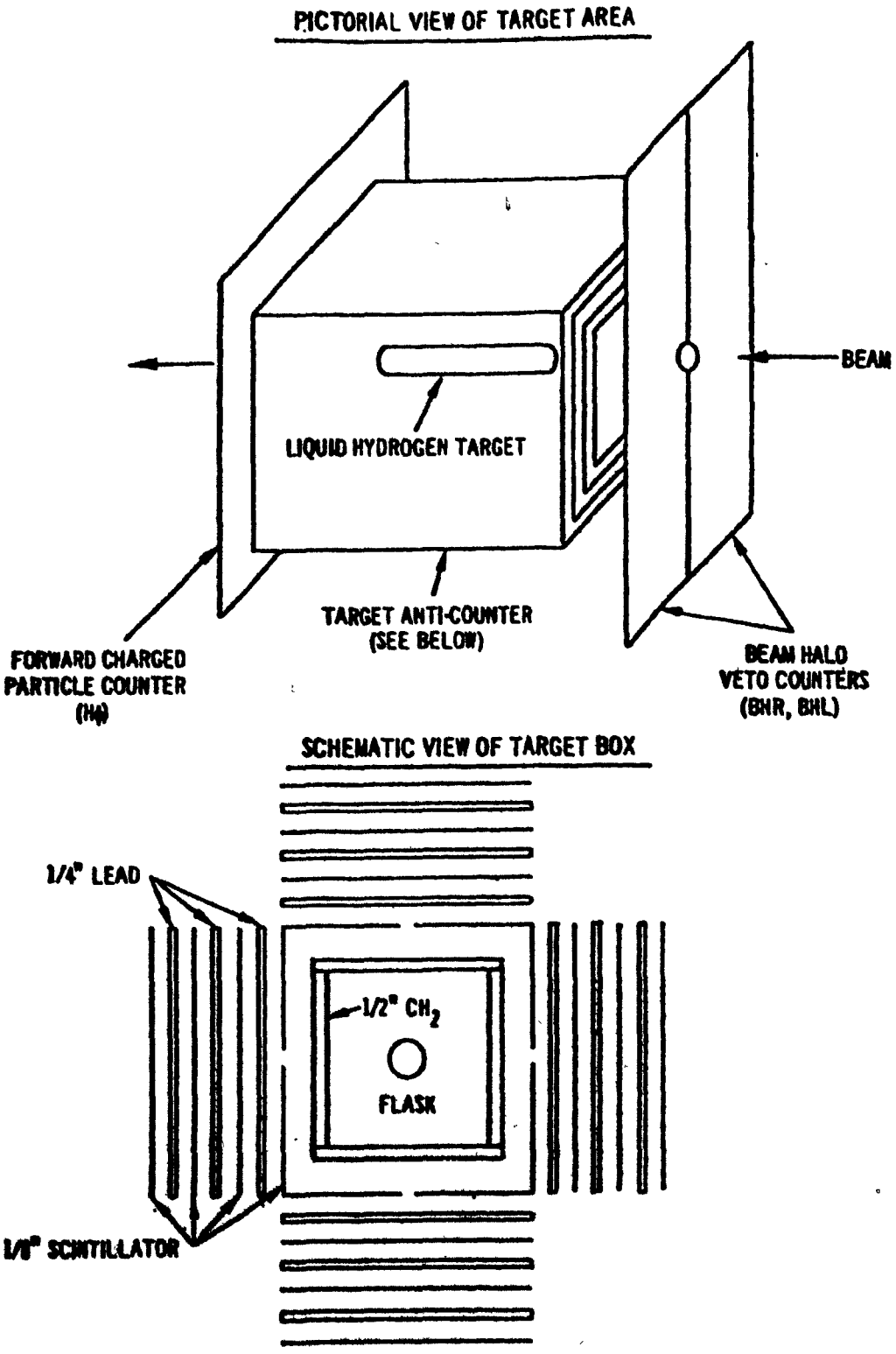

FIGURE 4 Target Anti-counter System

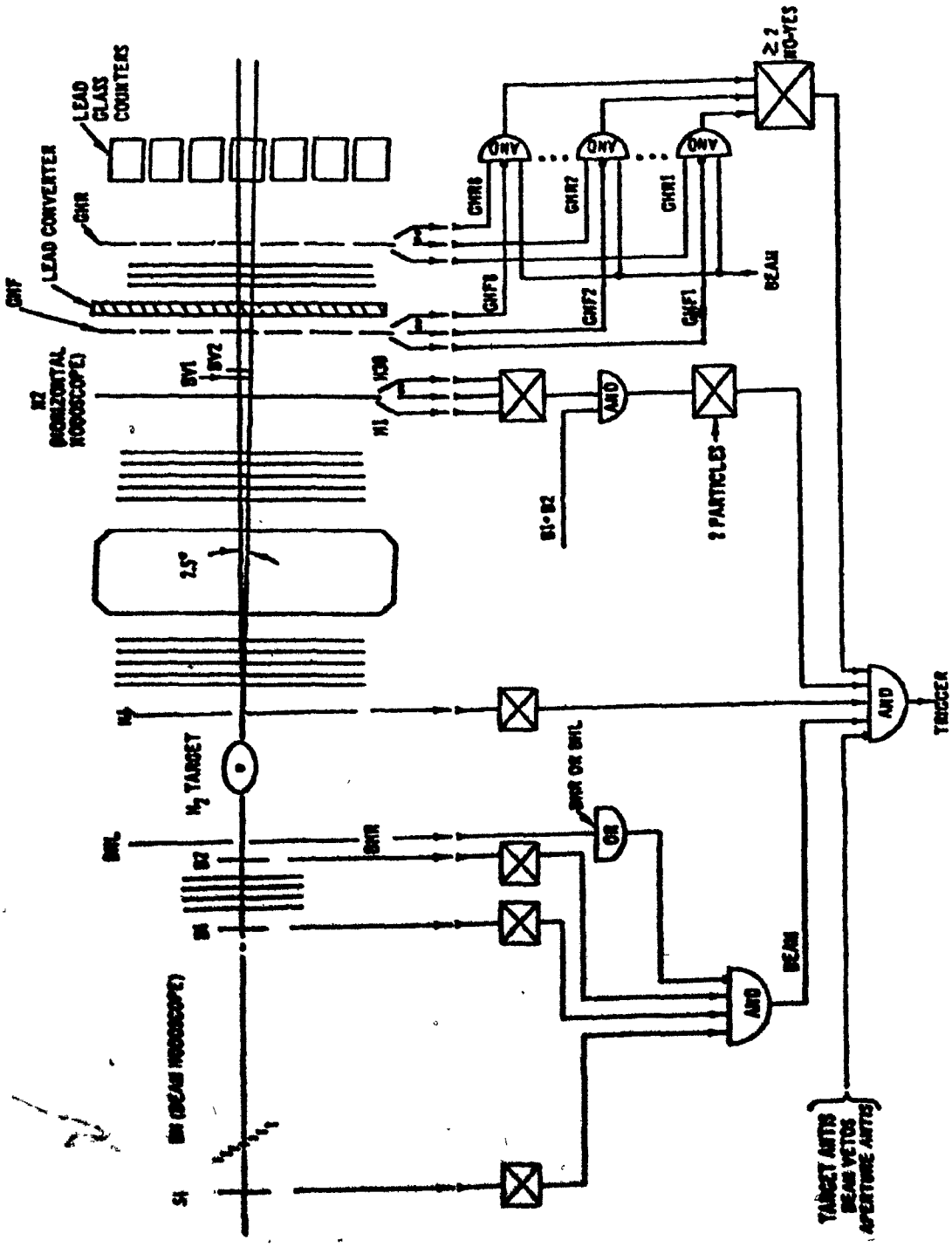

FIGURE 5 Trigger Schematic

1) Formation of Histogram for Block #N

A) Calculate Di-Gamma Mass For All Block #N Events

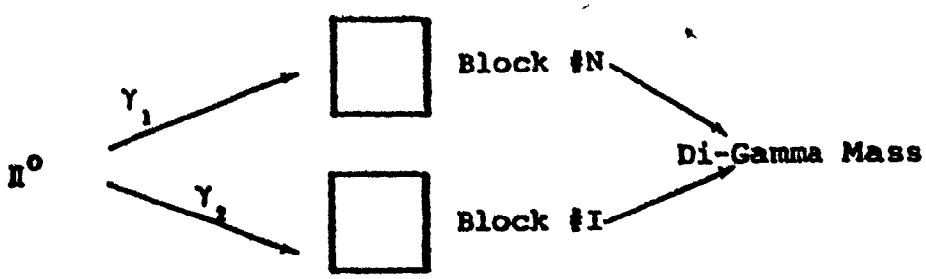

B) Sum Over All Blocks

$$\sum_{I=1}^{56}$$

C) Find Centroid Of Di-Gamma Mass Distribution And Compare With True π^0 Mass

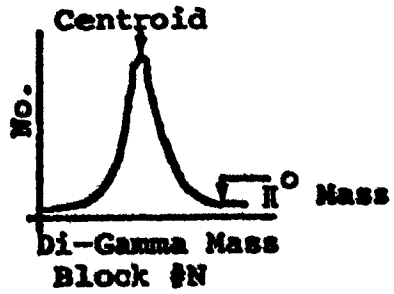

2) Correct Tube Gain For Block #N by Ratio

$$\left(\pi^0 \text{ Mass} \Big/ \text{Centroid Mass} \right)^{1/2}$$

FIGURE 6 Method for Lead Glass Energy Calibration

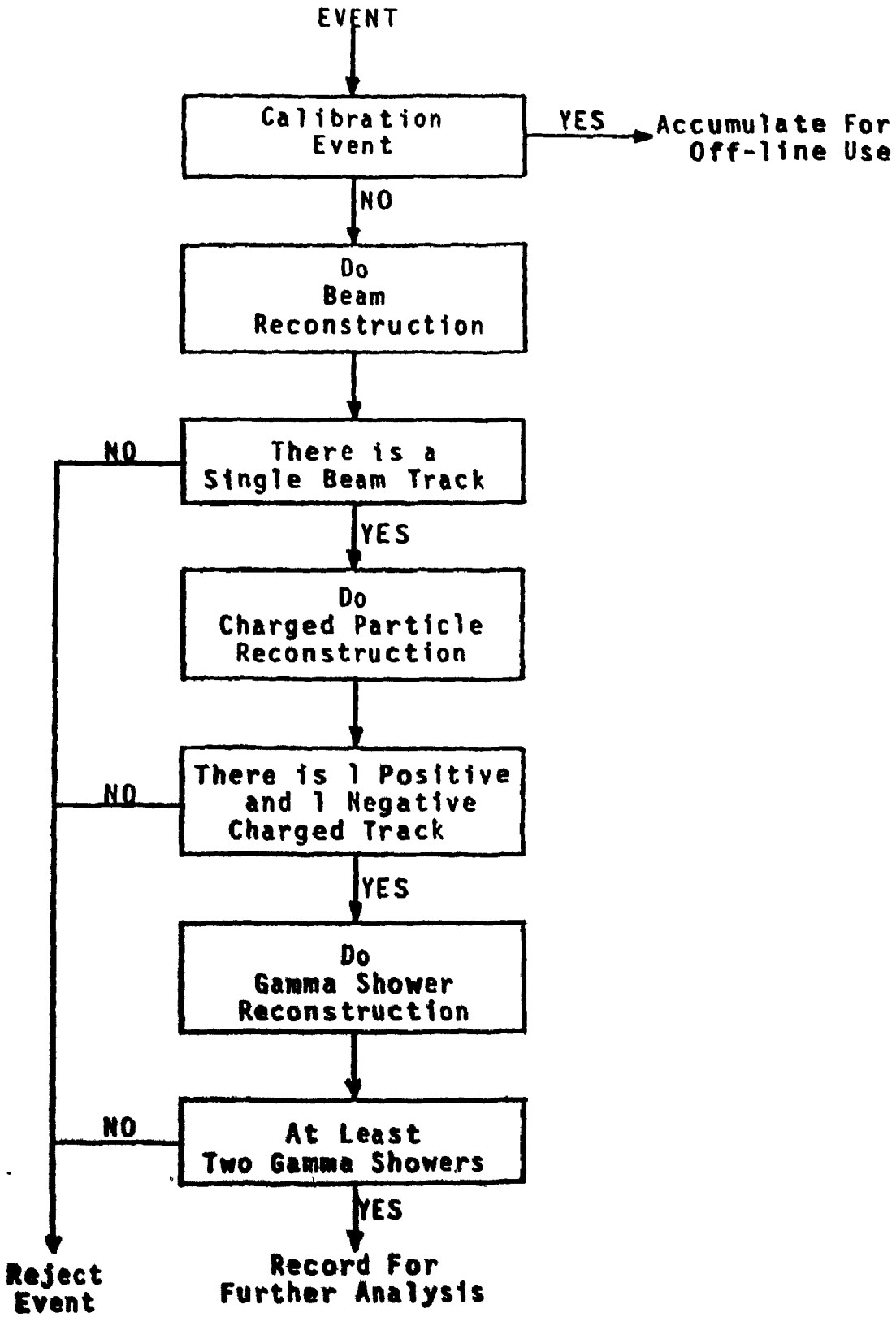

FIGURE 7 Software Reconstruction Analysis

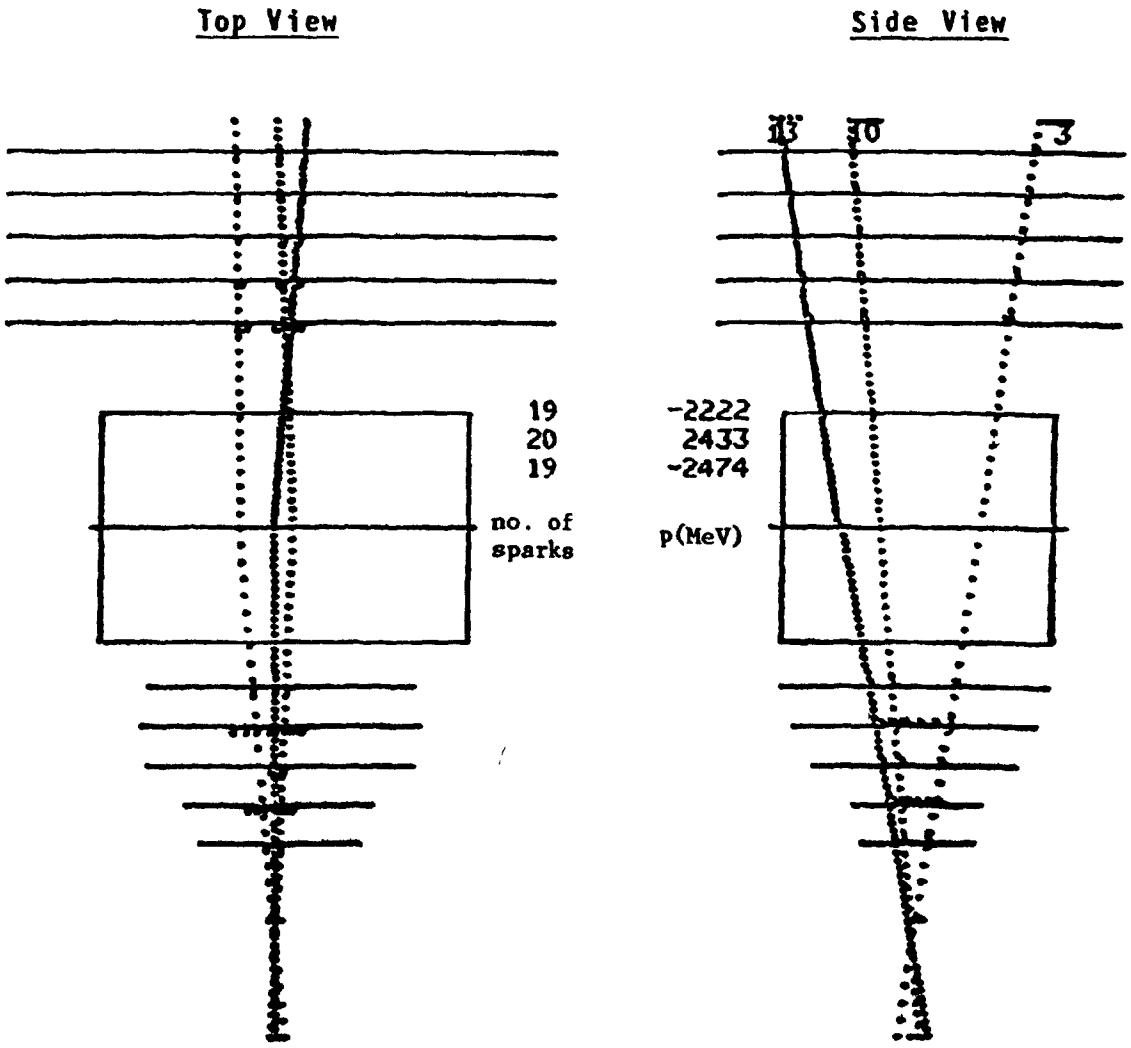

FIGURE 8 Example of a Reconstructed Three Prong Event

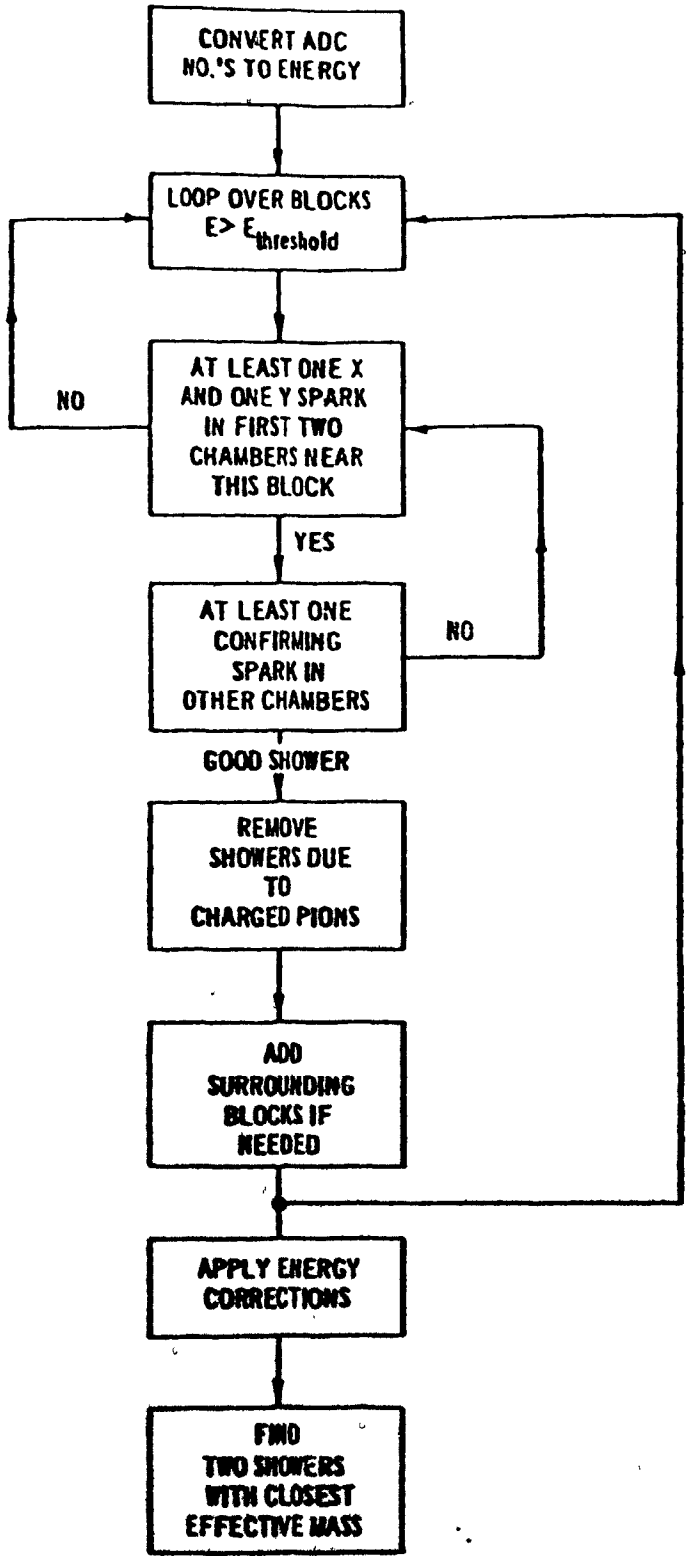

FIGURE 9 Gamma Shower Reconstruction Flowchart

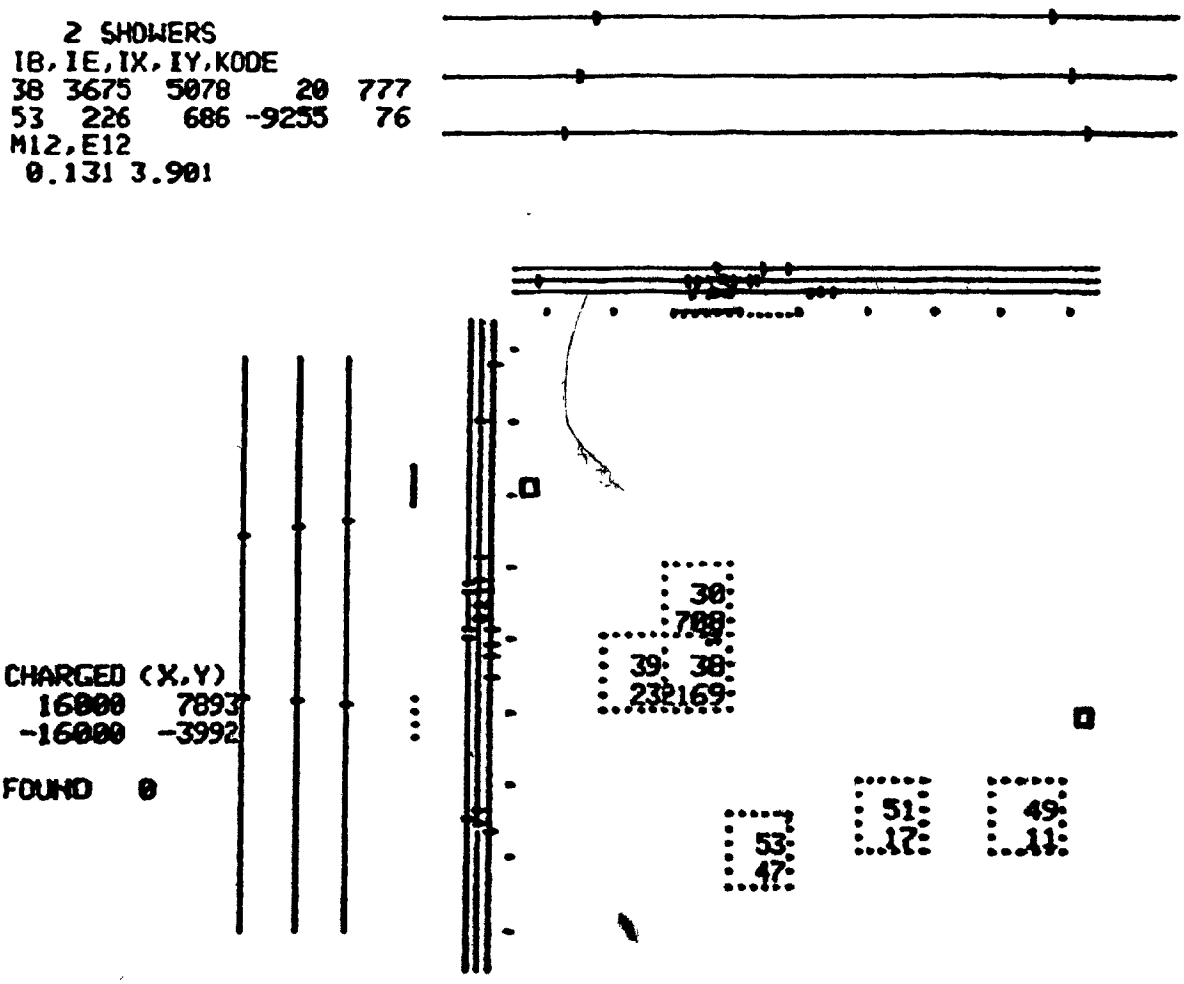

FIGURE 10 A Reconstructed 2γ Event

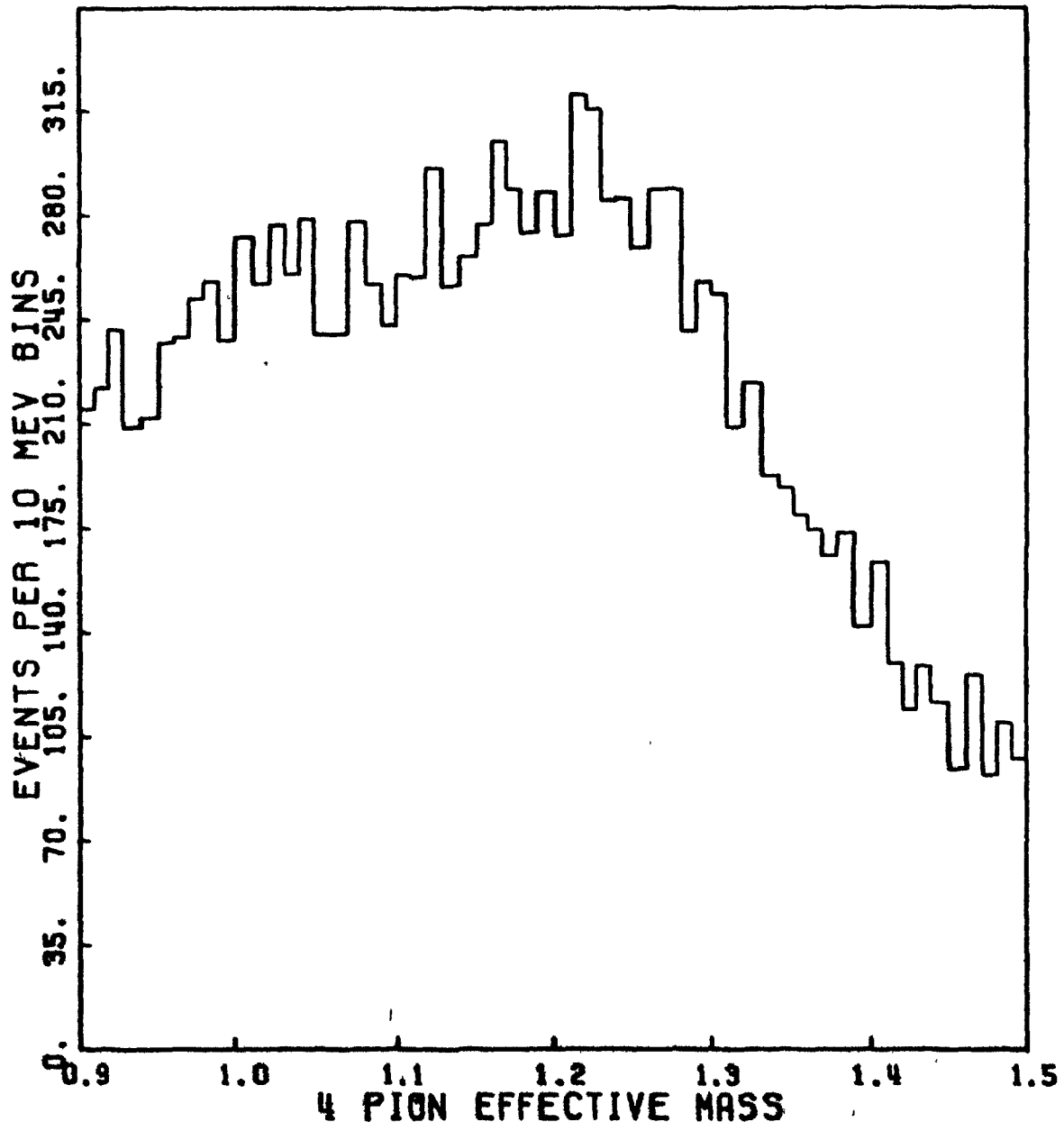

FIGURE 11 Initial 4π Sample

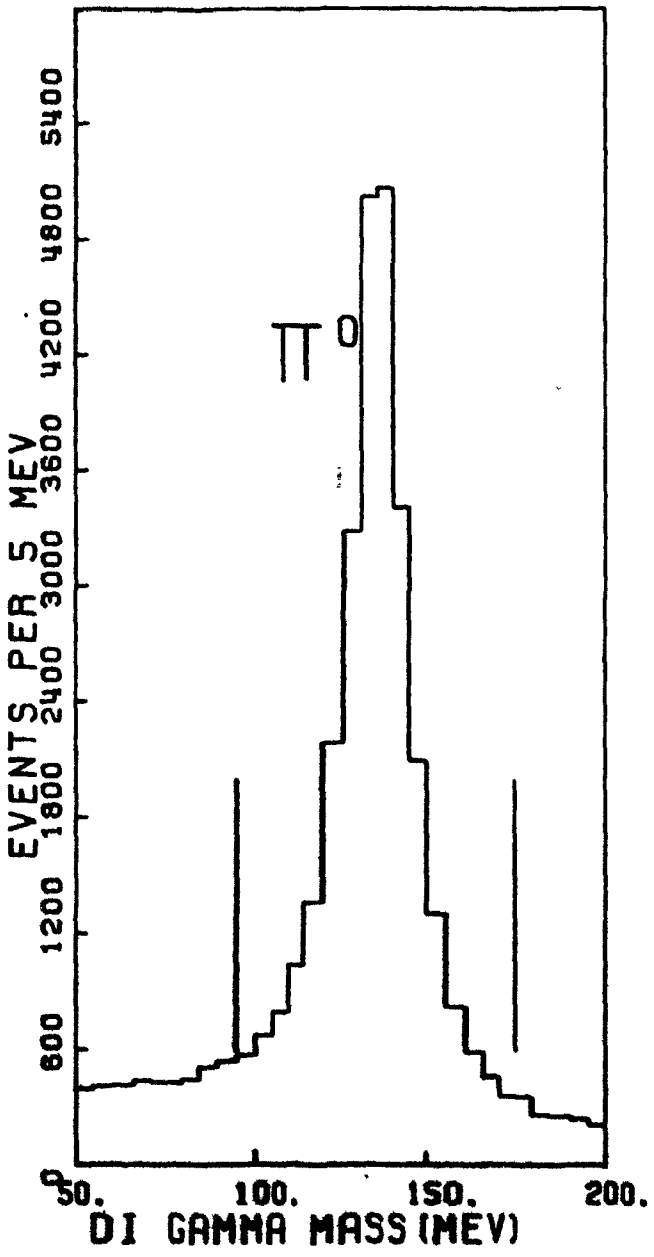

FIGURE 12 π^0 Effective Mass

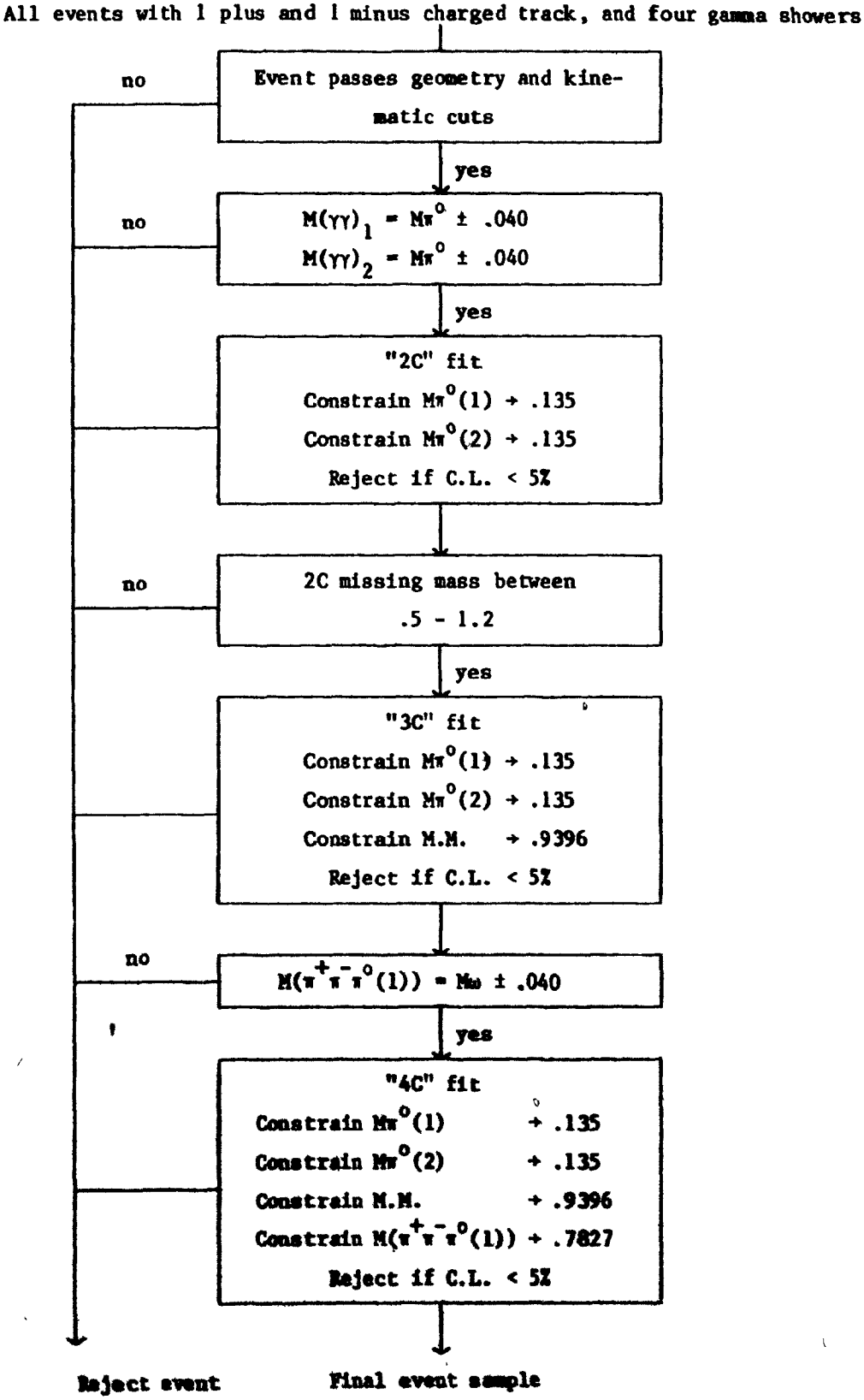

FIGURE 13 Kinematic Analysis Flowchart

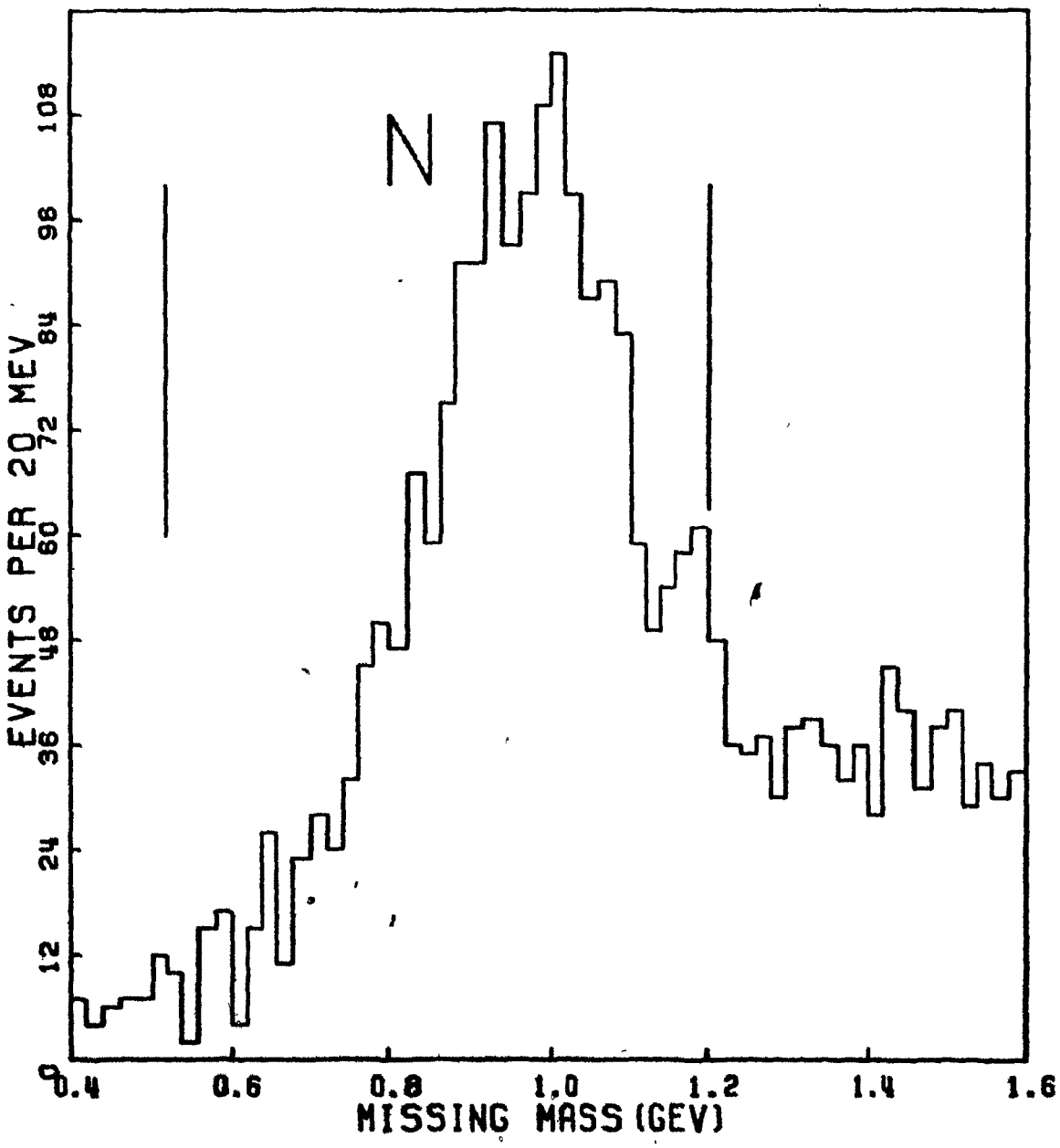

FIGURE 14a "2C" Missing Mass

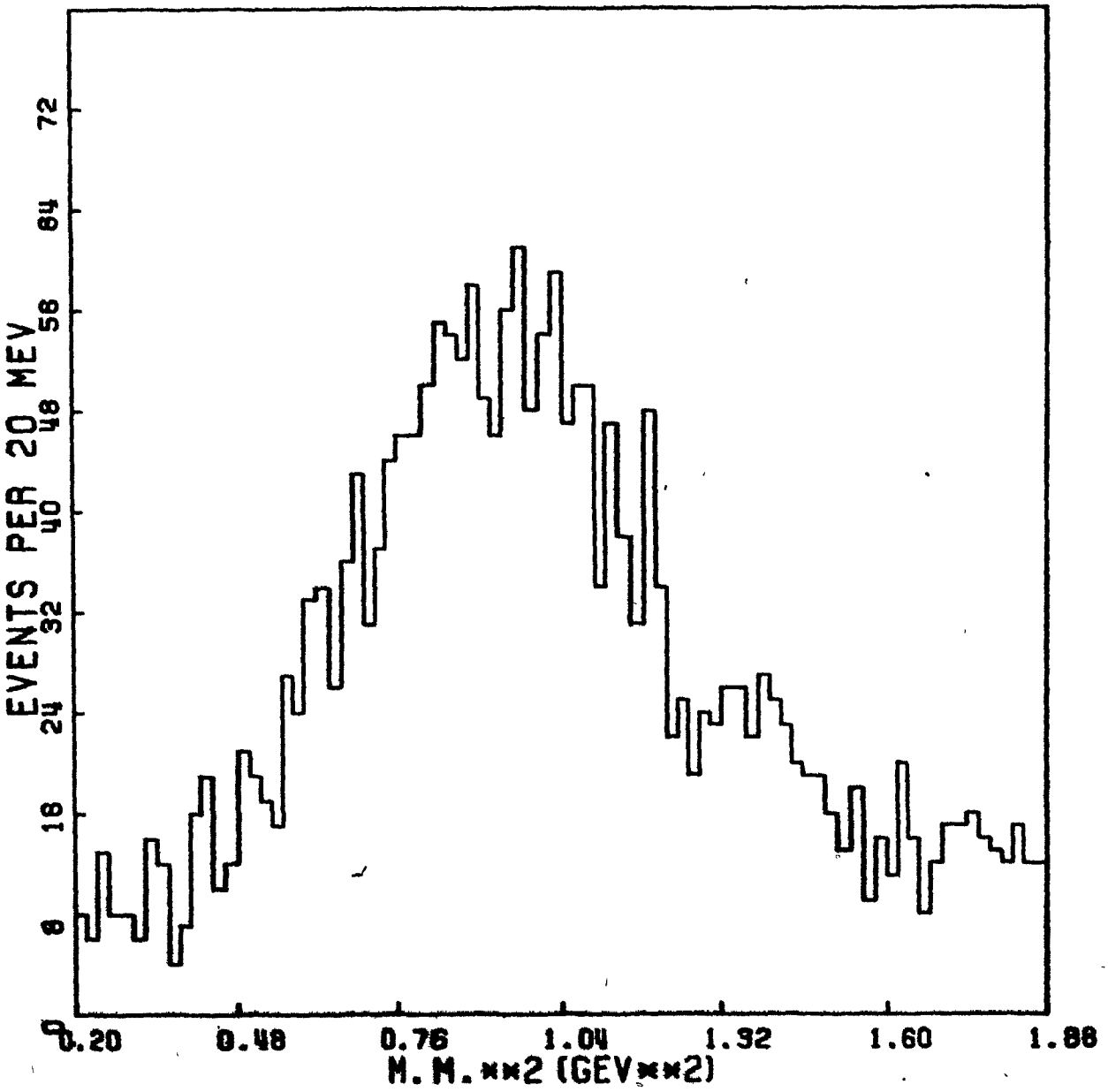

FIGURE 14b "2C" Missing Mass Squared

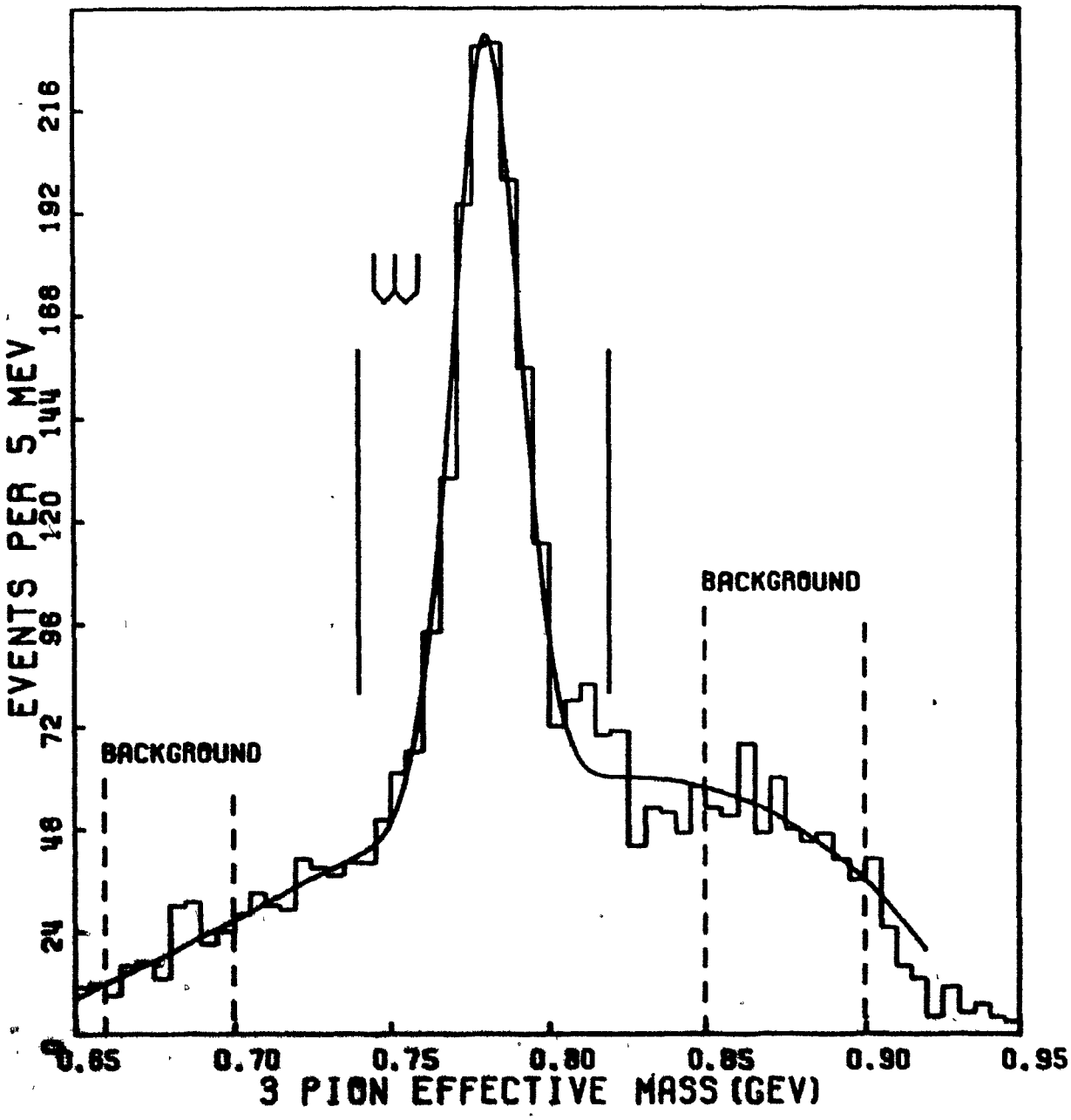

FIGURE 15 "3C" $\pi^+\pi^-\pi^0$(1) Effective Mass

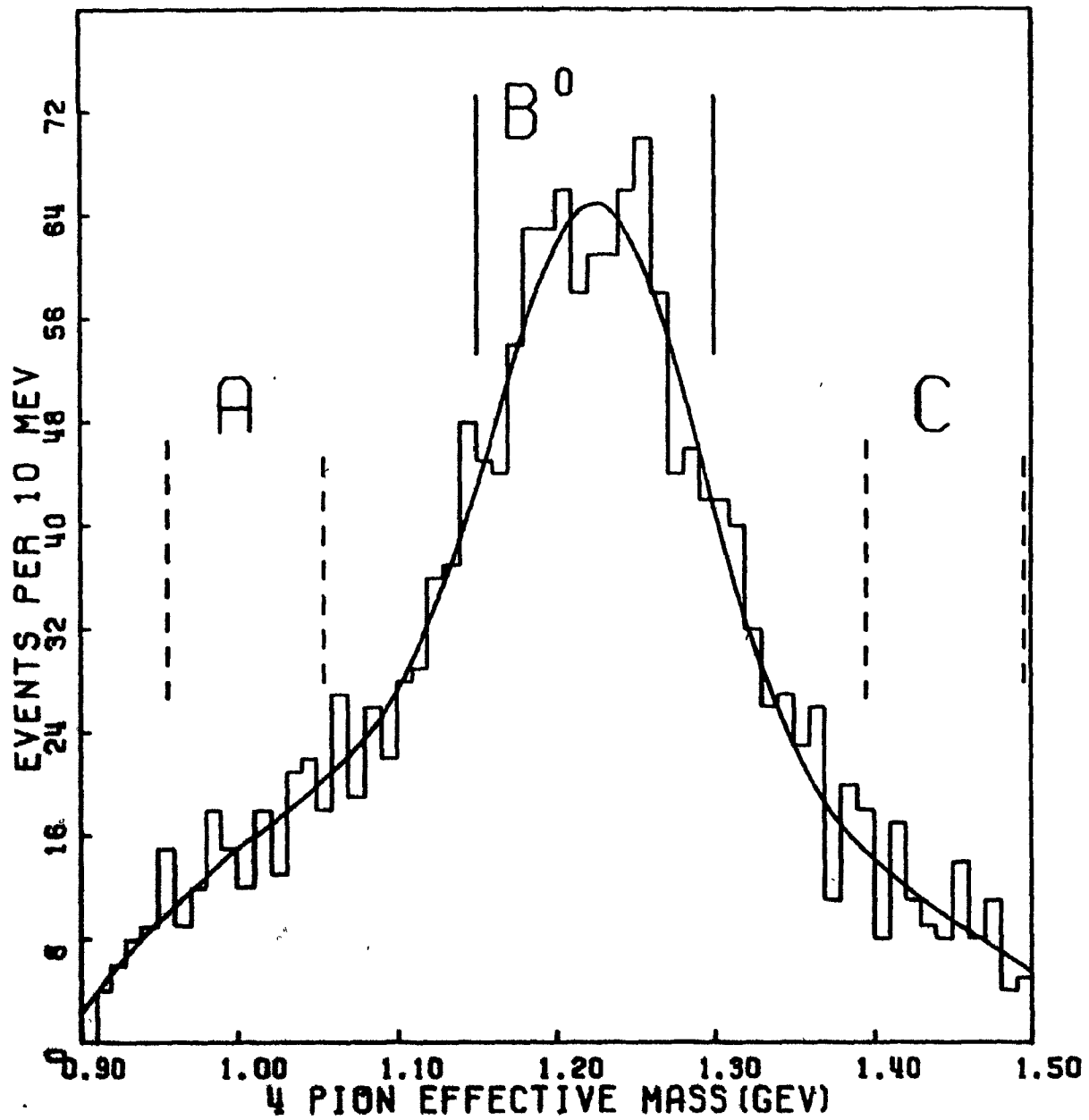

FIGURE 16 "4C" ω^0 Effective Mass

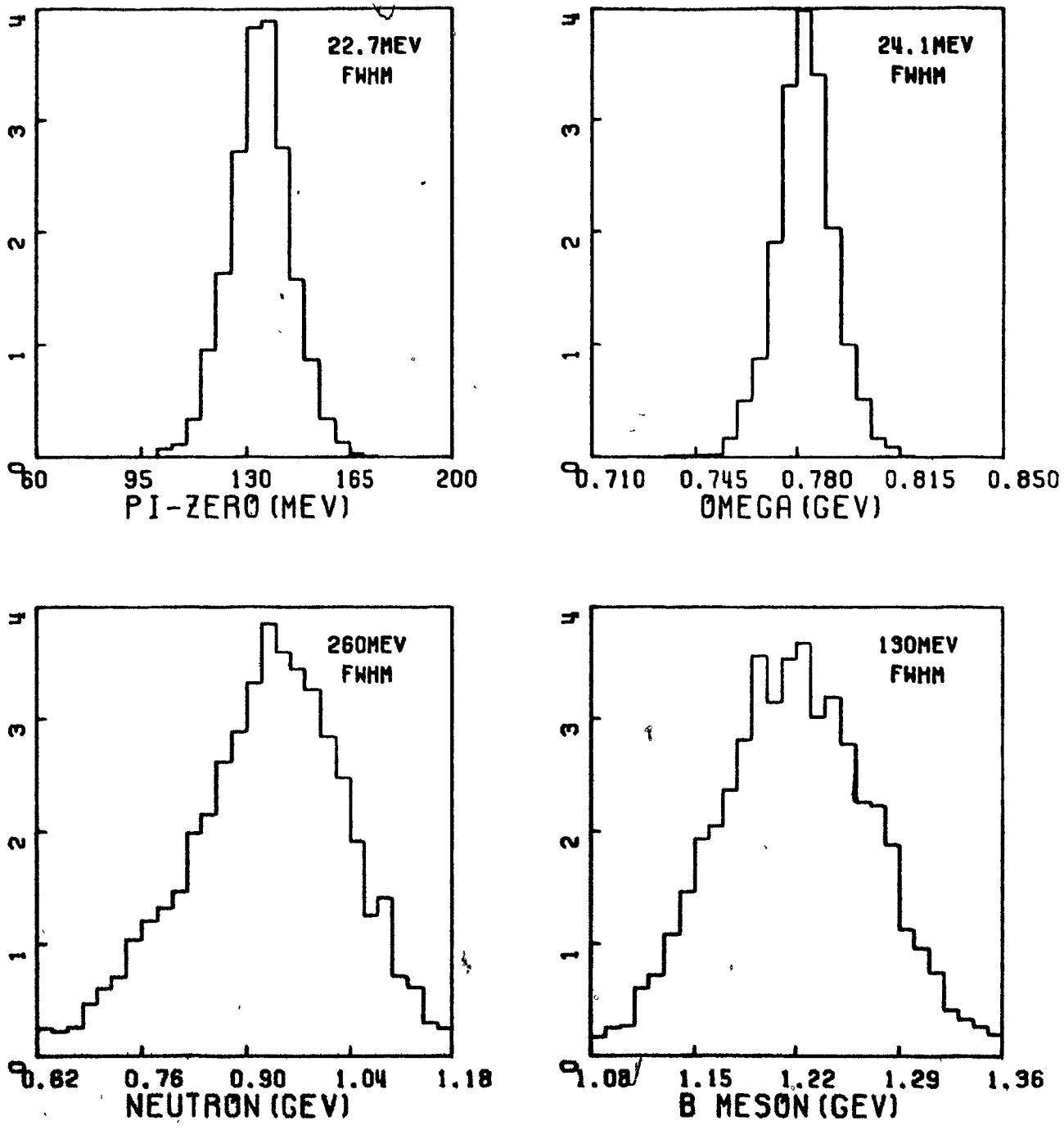

FIGURE 17 Resolution Functions

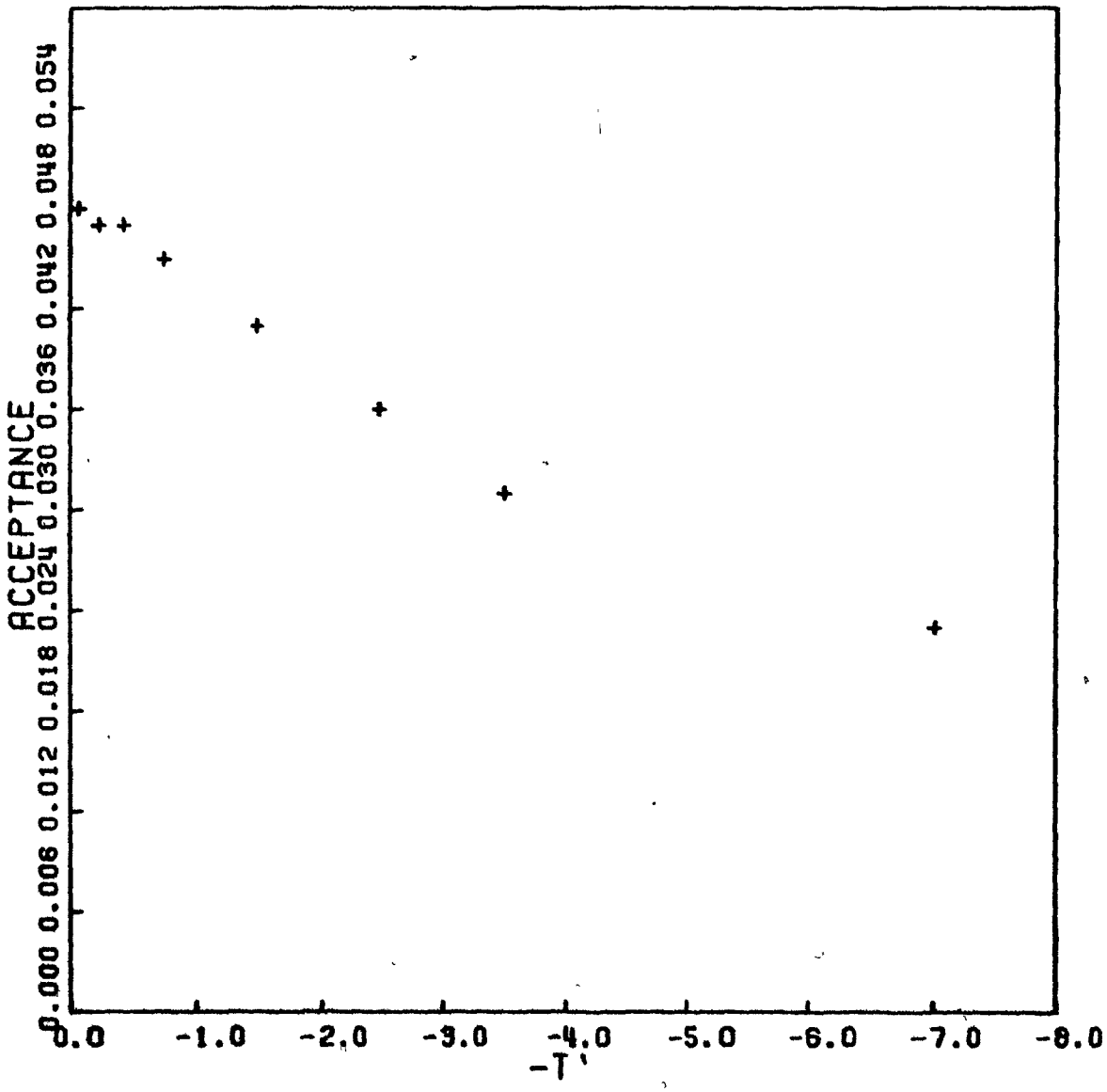

FIGURE 18 ω^0 Acceptance

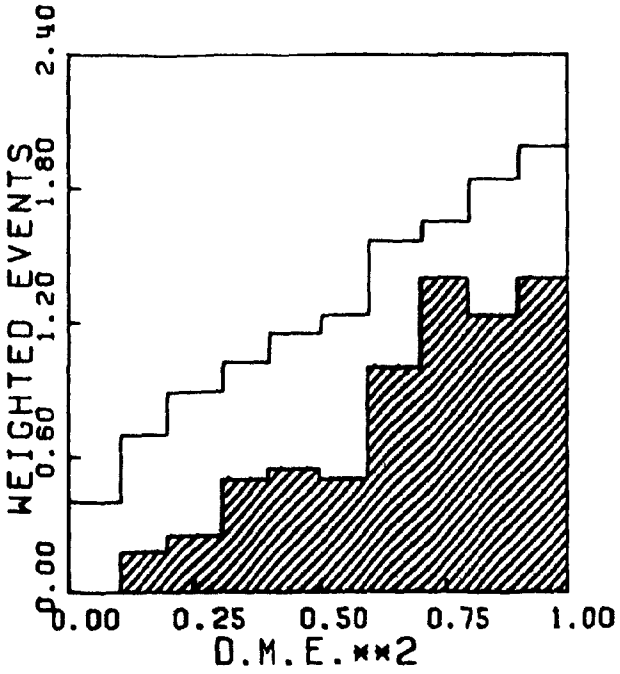

The top histogram includes all events in signal region, .740 - .820 GeV; shaded histogram includes all events, corrected for background with weight as per Breit-Wigner plus 4th order polynomial. It can be seen that the λ distribution after background subtraction is proportional to the distribution before subtraction, as expected for a pure ω sample.

FIGURE 19 λ

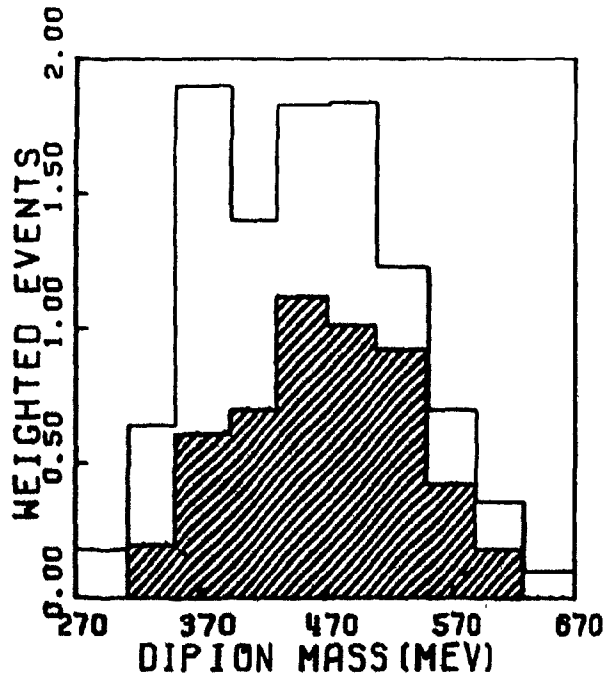

FIGURE 20a $M_{\pi^+\pi^-}$ (MeV)

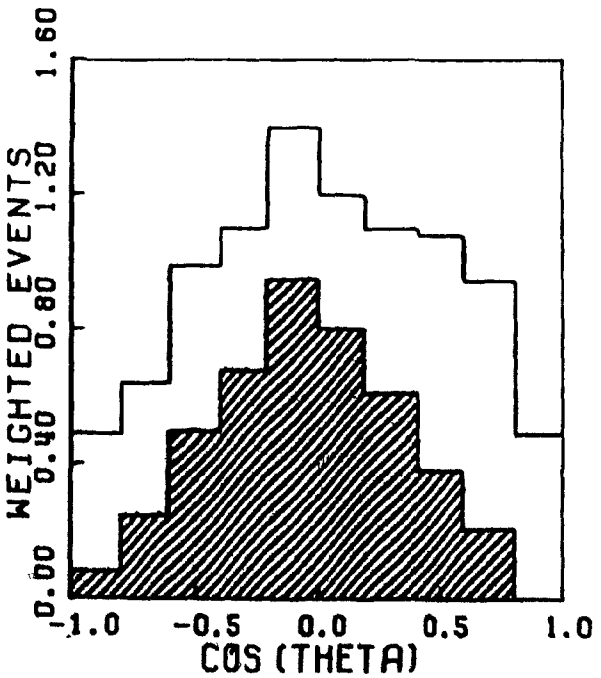

FIGURE 20b $\mu = \hat{p} \cdot \hat{q}$

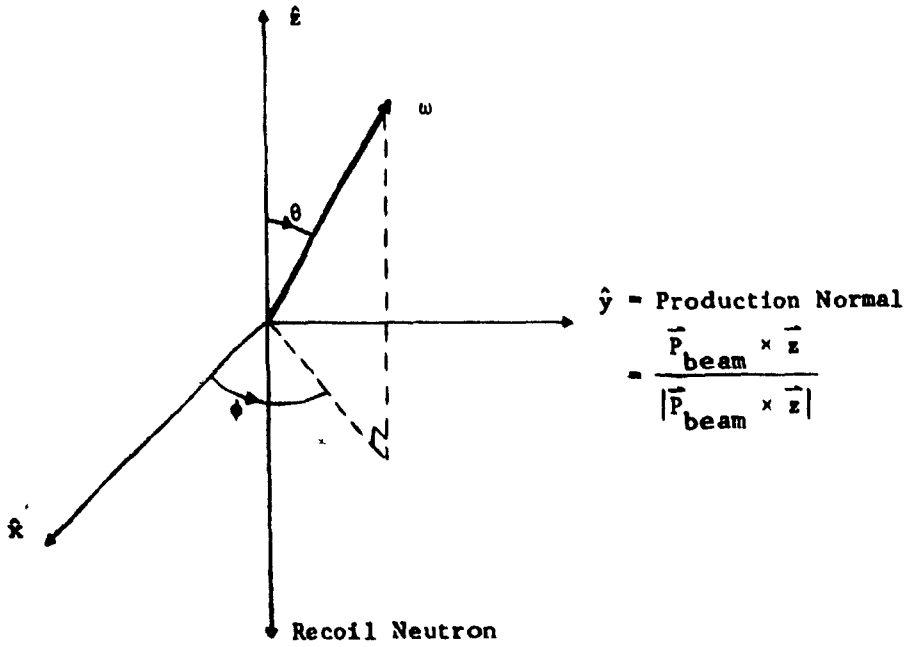

FIGURE 21a B^0 Helicity Rest Frame

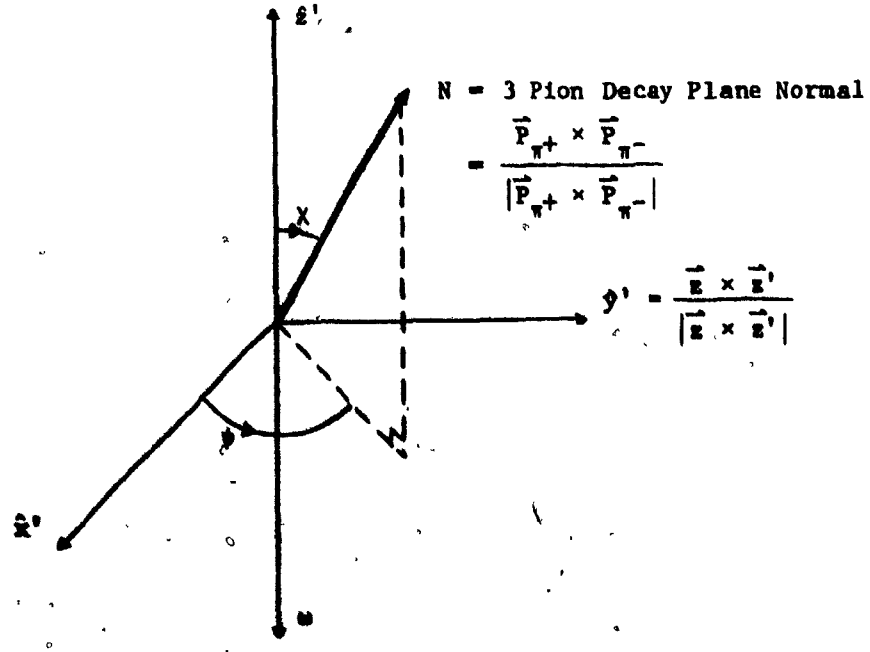

FIGURE 21b ω Helicity Rest Frame

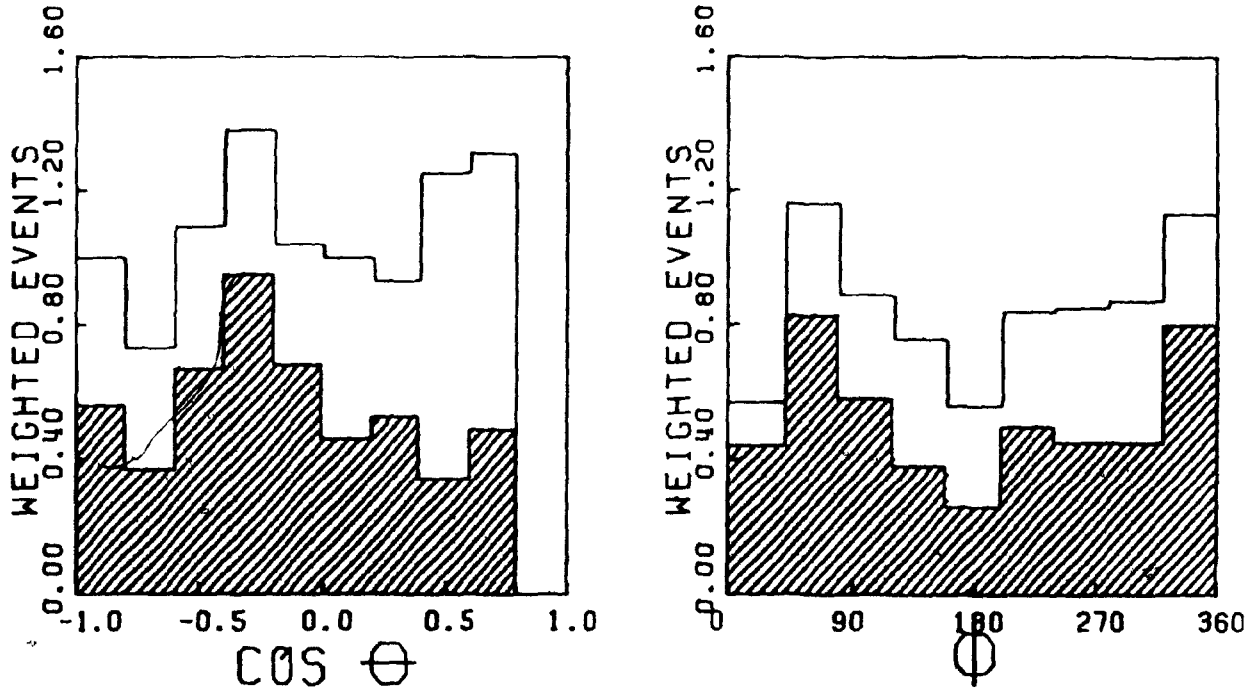

FIGURE 22 Angular Distributions of ω in B^0 Rest Frame

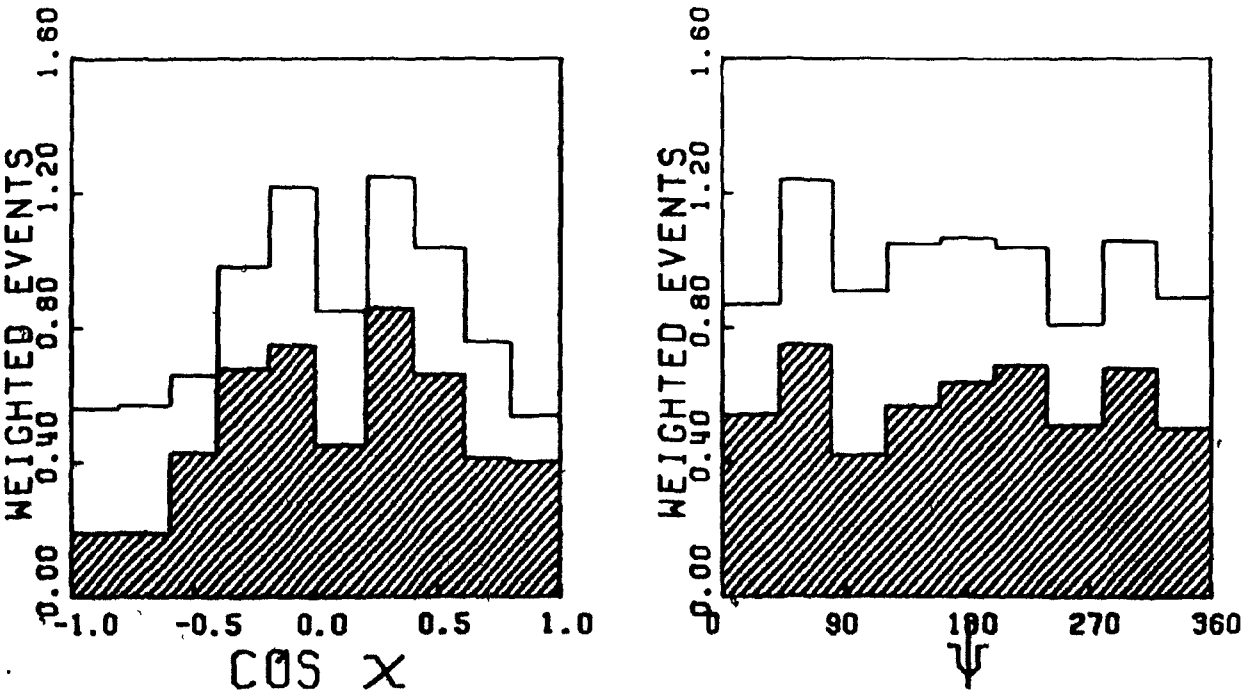

FIGURE 23 Angular Distributions of Normal to ω Decay Plane in ω Rest Frame

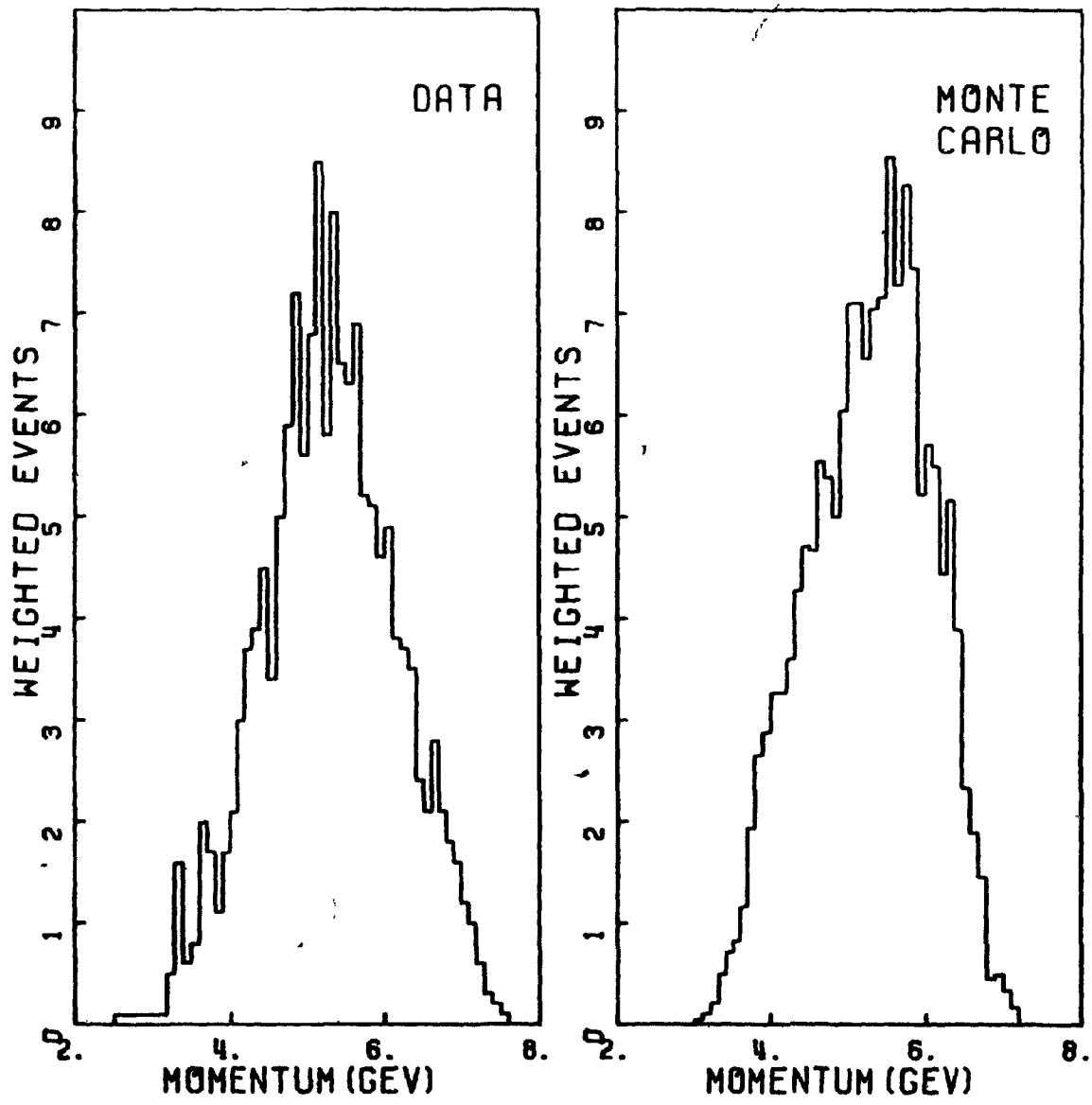

FIGURE 24a P_ω Data

FIGURE 24b P_ω Monte Carlo

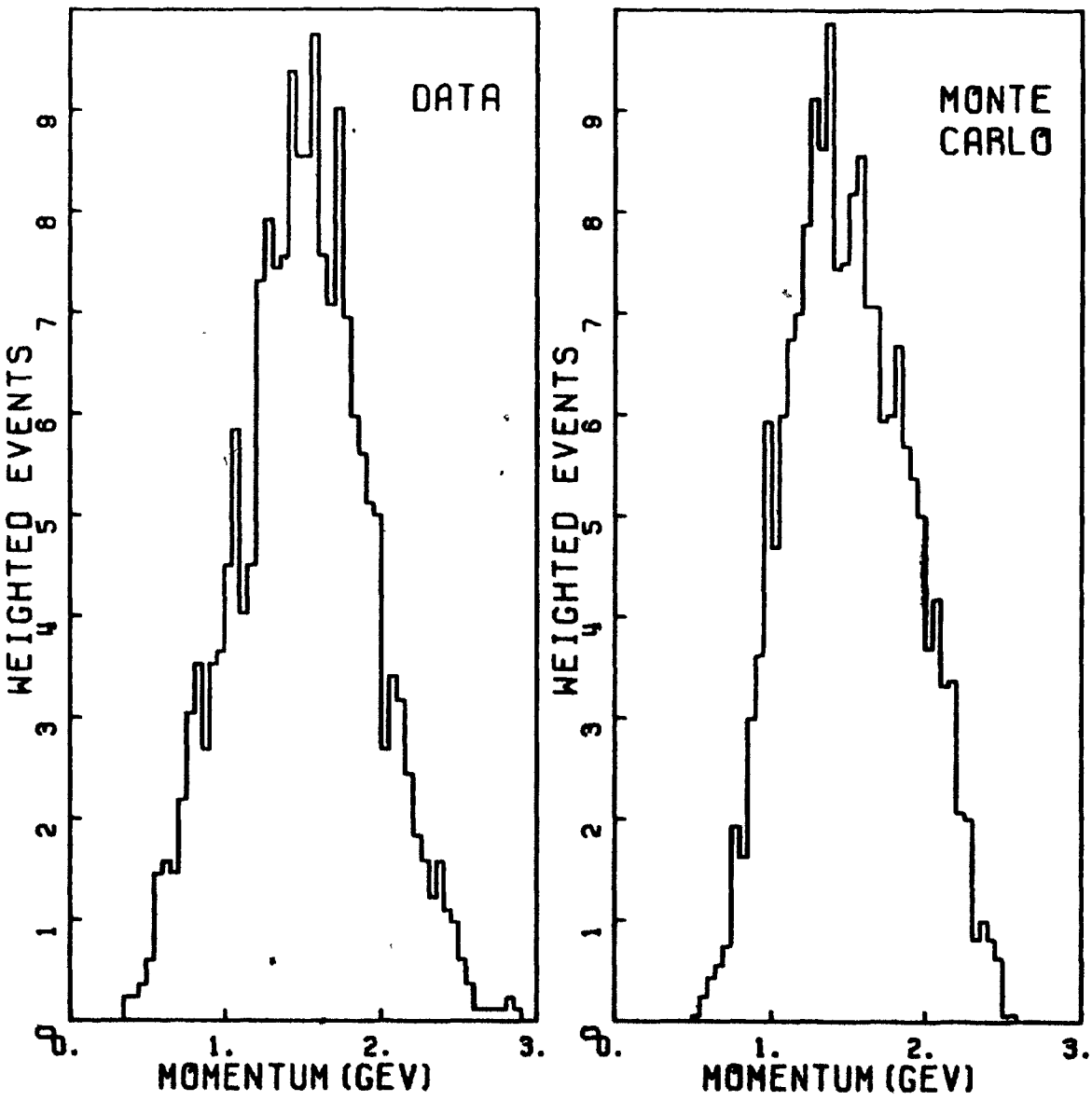

FIGURE 24c $P_{\pi^0(2)}$ Data

FIGURE 24d $P_{\pi^0(2)}$ Monte Carlo

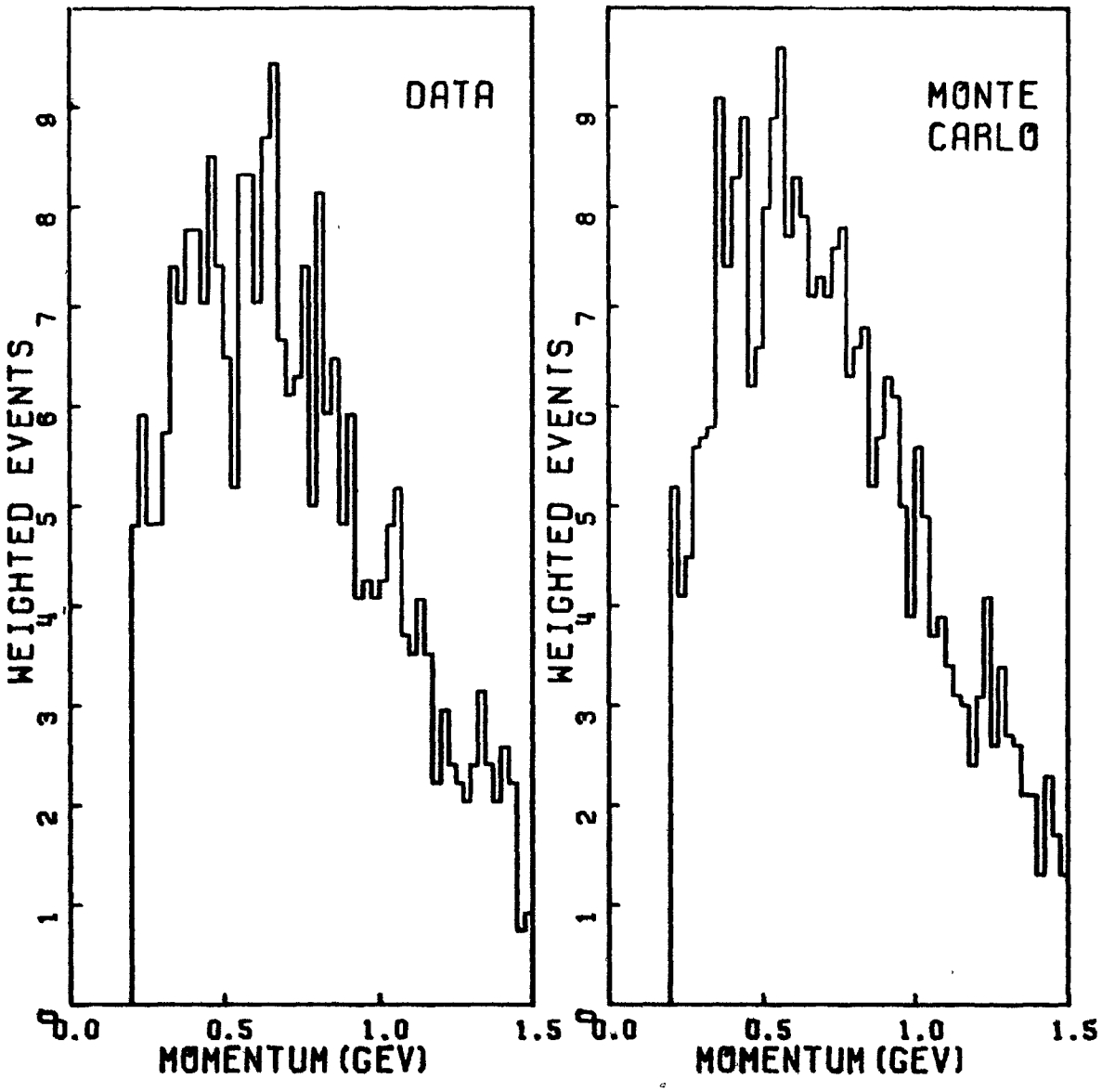

FIGURE 24e P_{π^+} Data

FIGURE 24f P_{π^+} Monte Carlo

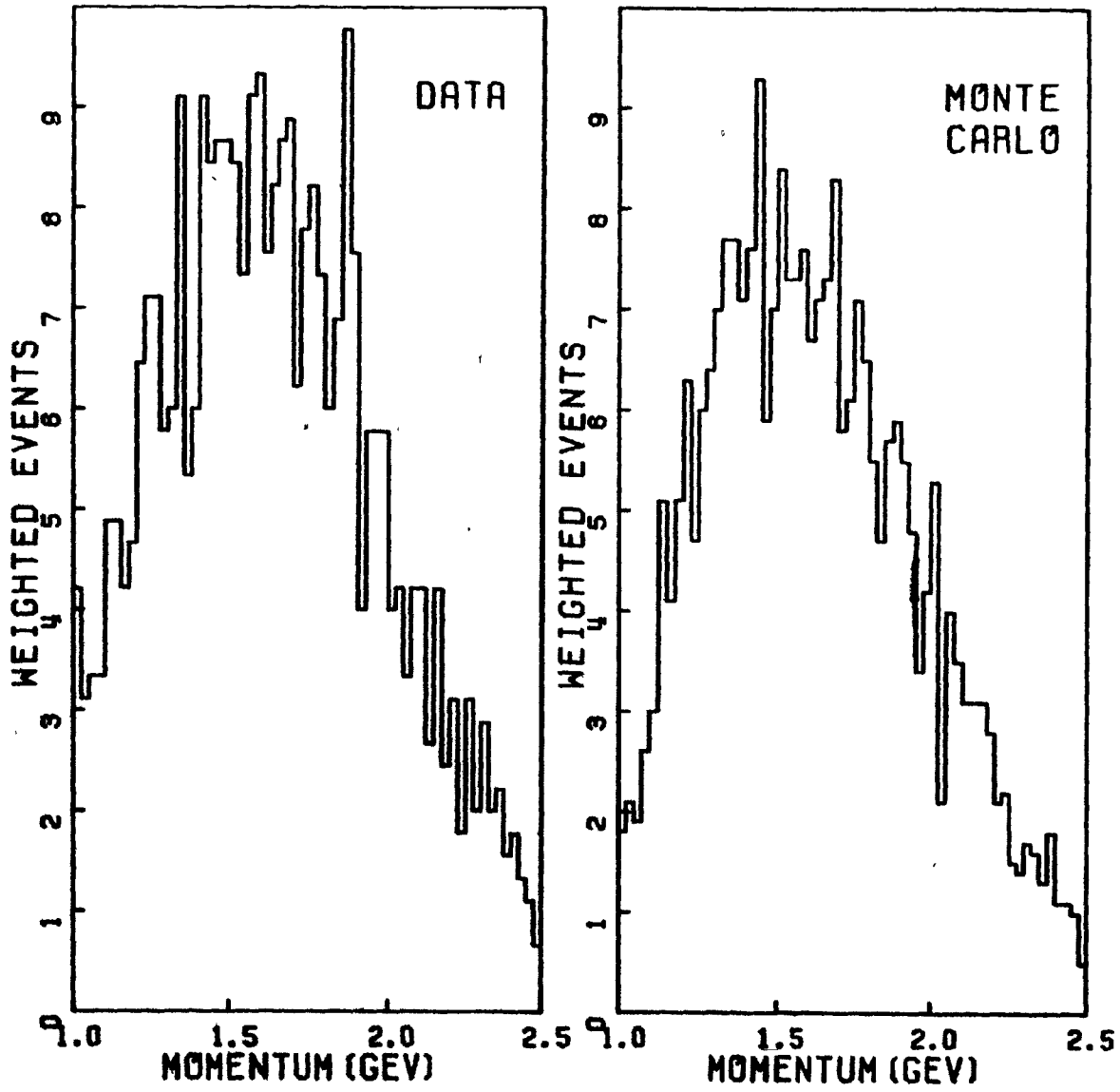

FIGURE 24g $P_{\pi^0_M}$ Data

FIGURE 24h $P_{\pi^0_M}$ Monte Carlo

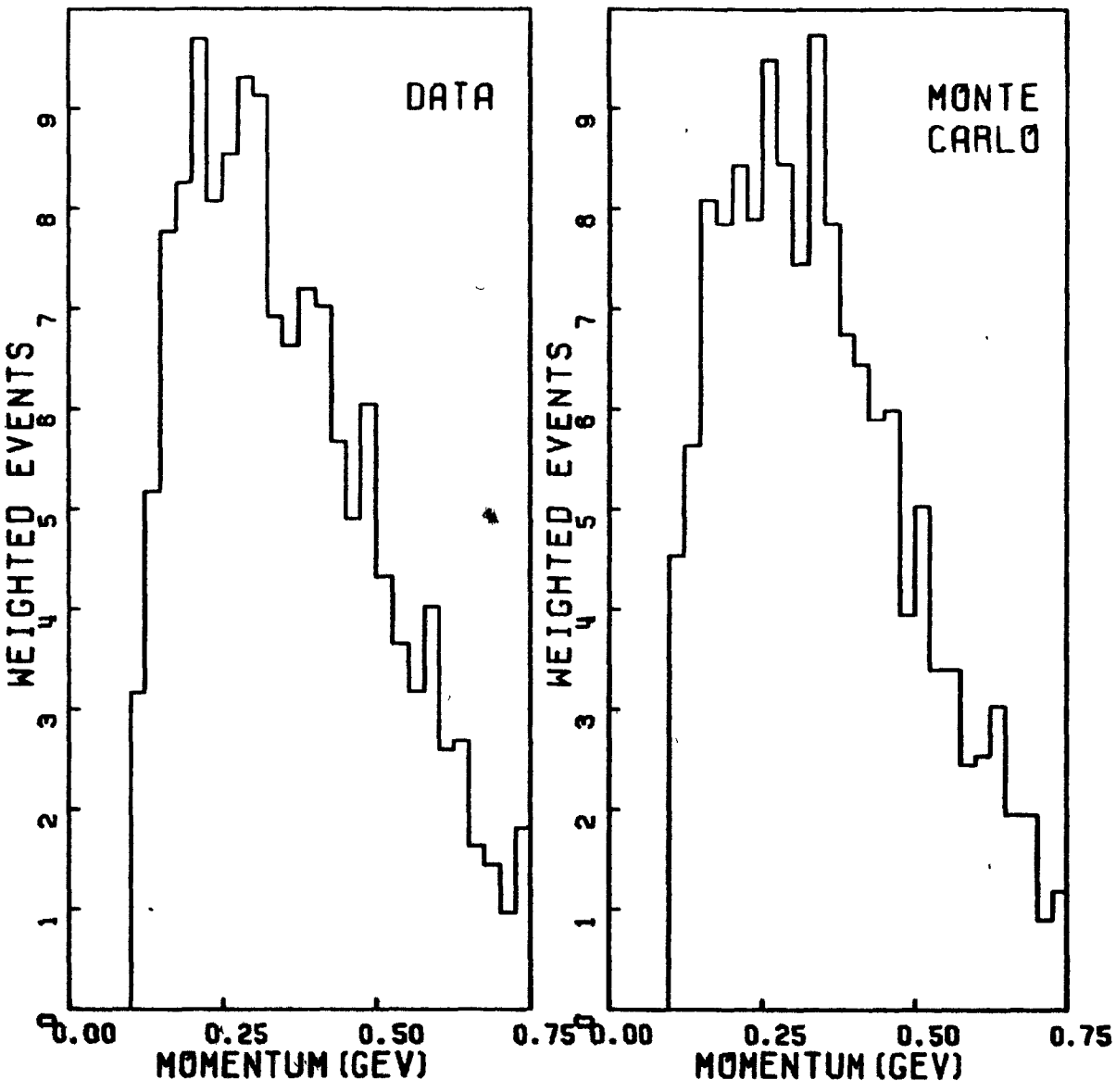

FIGURE 24i P_{Y_2} Data

FIGURE 24j P_{Y_2} Monte Carlo

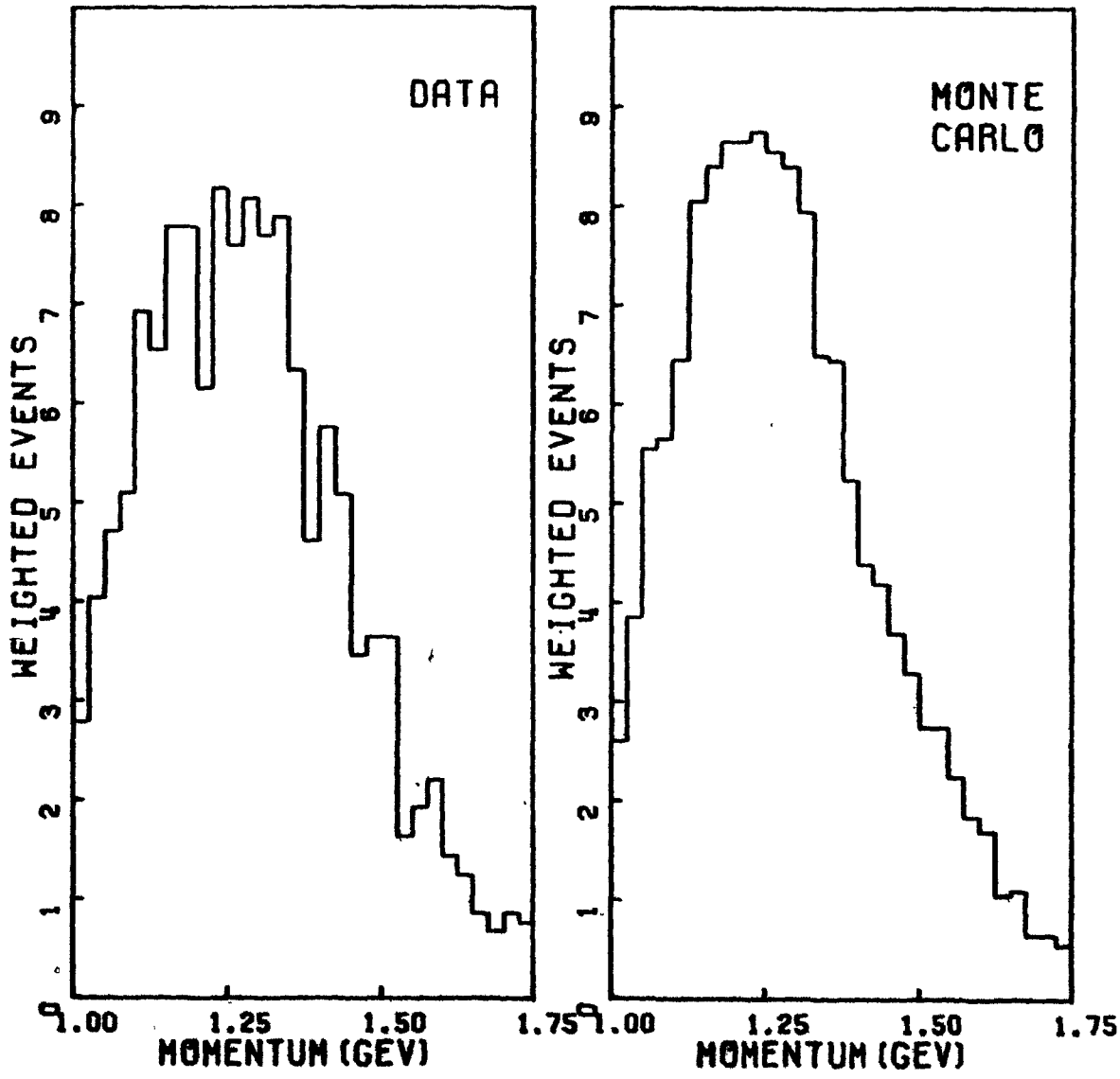

FIGURE 24k P_{Y_3} Data

FIGURE 241 P_{Y_3} Monte Carlo

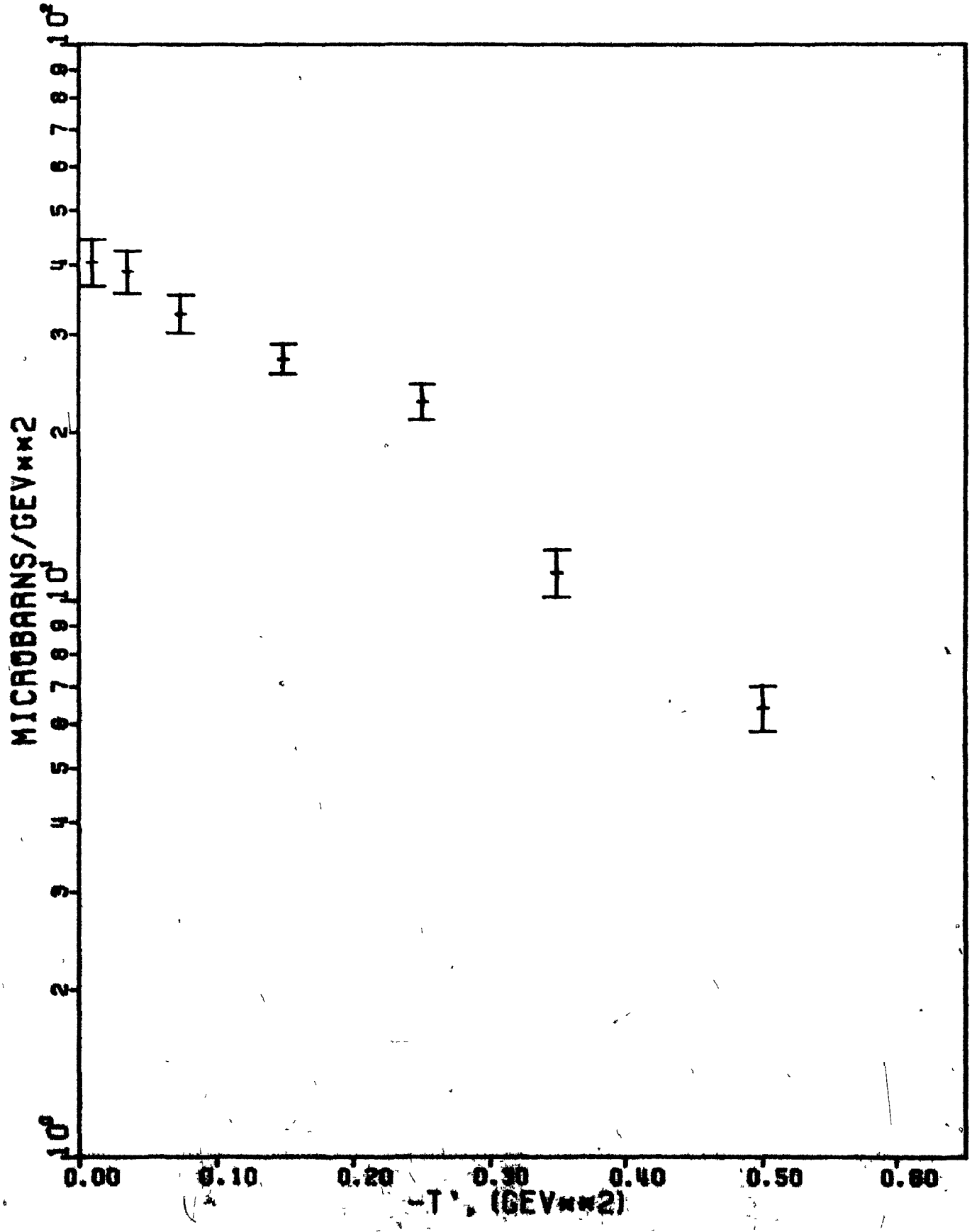
MICROBARNS/GEV**2
10²
9
8
7
6
5
4
3
2
10¹
9
8
7
6
5
4
3
2
10⁰
0.00
0.10
0.20
0.30
0.40
0.50
0.60
-T', (GEV**2)